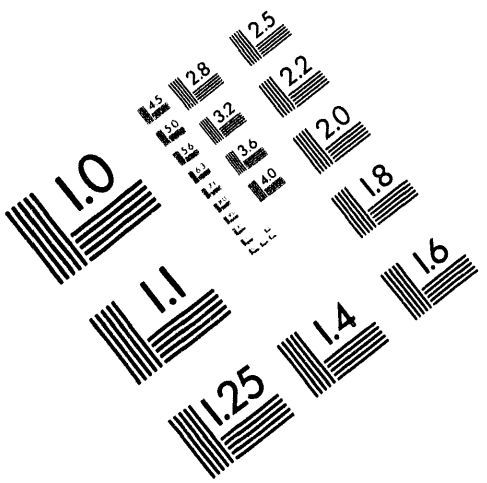

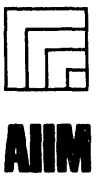

Association for Information and Image Management

1100 Wayne Avenue, Suite 1100
Silver Spring, Maryland 20910

301/587-8202

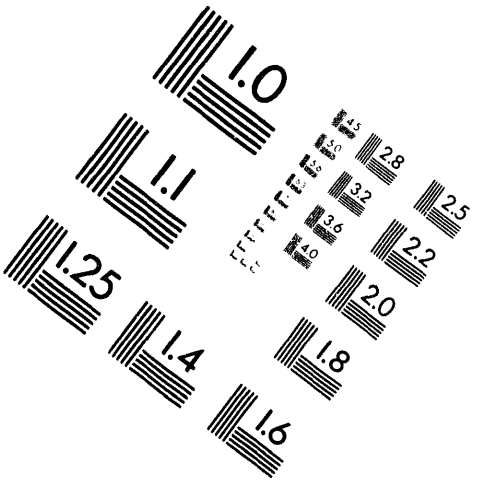

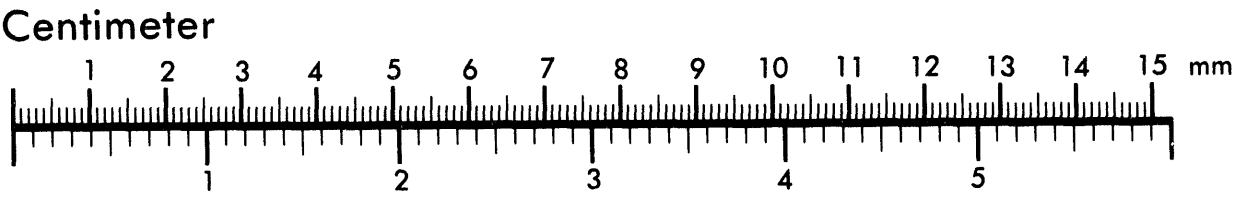

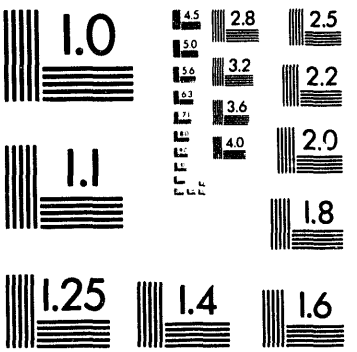

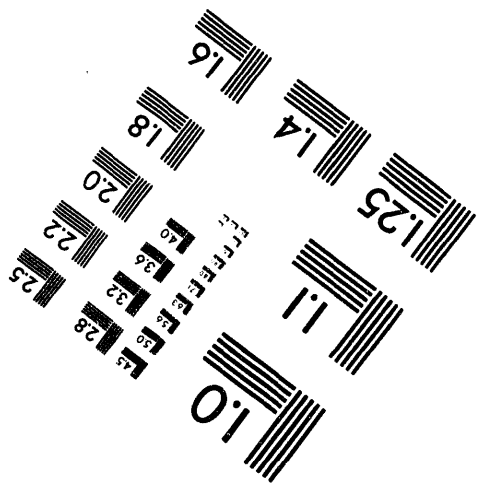

MANUFACTURED TO AIIM STANDARDS
BY APPLIED IMAGE, INC.

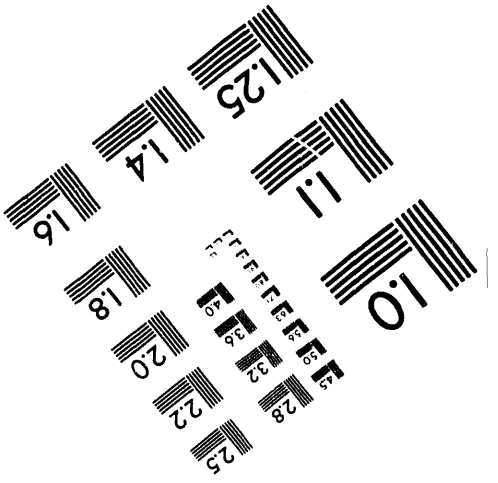

1 of 1

LA-UR-94-2249

Los Alamos National Laboratory is operated by the University of California for the United States Department of Energy under contract W-7405-ENG-36

TITLE: APT RADIONUCLUDE PRODUCTION EXPERIMENT

AUTHOR(S): John L. Ullmann, Avigdor Gavron, Joe D. King, Richard Laird, Doug Mayo, Laurie Waters, Christoph Zoeller, Parrish Staples, Daniel Jagnow, James E. Koster, Paul W. Lisowski, Ron O. Nelson, Stephen A. Wender, Gil Butler, Russell E. Gritzo, Mary Ann Yates, Malcolm Fowler, Jerry Wilhelmy, and William Wilson

SUBMITTED TO: US Department of Energy
Office of Weapons Complex Reconfiguration, DP-40

DISCLAIMER

Los Alamos
Los Alamos National Laboratory
Los Alamos, New Mexico 87545

FORM NO. 836 R4
ST NO 2629 5/91

MASTER

LOS ALAMOS NATIONAL LABORATORY

ACCELERATOR PRODUCTION OF TRITIUM PROJECT

TECHNICAL REPORT

APT RADIONUCLIDE PRODUCTION EXPERIMENT

Submitted to the US Department of Energy
Office of Weapons Complex Reconfiguration, DP-40

Participants

Group P-17

J.L. Ullmann
A. Gavron
J. King
R. Laird
D. Mayo
L. Waters
C. Zoeller
P. Staples
D. Jagnow
J. Koster
P.W. Lisowski
R.O. Nelson
S.A. Wender

Group INC-13

G. Butler
R. Gritzo
M.A. Yates
M. Fowler
J. Wilhelmy

Group T-2

W. Wilson

1. Introduction

Tritium (^{3}H, a heavy isotope of hydrogen) is produced by low energy neutron-induced reactions on various elements. One such reaction is $n+^3He \rightarrow ^3H+^1H$ in which ^{3}He is transmuted to tritium. Another reaction, which has been used in reactor production of tritium, is the $n+^6Li \rightarrow ^3H+^4He$ reaction. Accelerator Production of Tritium relies on a high-energy proton beam to produce these neutrons using the spallation reaction, in which high-energy protons reacting with a heavy nucleus produce a shower of low-energy neutrons and a lower-mass residual nucleus. It is important to quantify the residual radionuclides produced in the spallation target for two reasons. From an engineering point of view, one must understand short-lived isotopes that may contribute to decay heat. From a safety viewpoint, one must understand what nuclei and decay gammas are produced in order to design adequate shielding, to estimate ultimate waste disposal problems, and to predict possible effects due to accidental dispersion during operation.

Because stopping-length targets (i.e. targets in which the initial protons will lose all their energy prior to coming to a stop) will be used for neutron production, radionuclide production over a wide energy range must be considered. The calculation of radionuclide production in a thick target involves two different processes. First, the transport of the incident particles and their reaction products, including neutrons, must be considered in detail. Second, the probability for production of a given radionuclide in a reaction must be calculated.

Although numerous measurements of thin-target radionuclide production have been made, there have been only a few measurements of stopping-length systems [1,2]. The most complete study, described in [1], showed results for Pb and U targets, but was not completely analyzed or published.

The design of targets for neutron production using spallation involves elaborate calculations with Monte-Carlo transport and particle production codes. These codes follow every particle produced until it either slows down to the point of stopping, or vanishes due to the interaction with an atomic nucleus. This tracking takes place through elaborate geometric structures involving many different materials. The probability that a particle will interact at any point in a material is determined by its "cross-section". The cross-section is a characteristic property of each nucleus, and varies with the energy and the species (i.e., proton, neutron,...) of the impinging particle. When a particle interacts, other particles may be produced or the incoming particle may be scattered to a new direction. The probability for a particle to interact and produce one or more particles in a given direction and with a given energy is termed a "double-differential" cross-section, and denoted $d^2\sigma/dEd\Omega$. These cross-sections need to be known for all the elements and for all particles and energies that could be produced in a spallation target in order to be able to accurately track the initial particle and the subsequent generations of particles produced in a target. For neutrons up to energies of

20 MeV, numerous measurements of $d^2\sigma/dEd\Omega$ have been made. They have been incorporated in vast libraries used by the MCNP (Monte-Carlo Neutron and Photon) code for tracking neutrons [3].

Very few measurements of the double-differential cross section have been made for neutrons at higher energies, or for all other particles. The current status of experimental data is discussed in several reviews [4,5,6,7]. Where cross sections are not available, the calculations use physics models. One such model, the Intra-Nuclear Cascade (INC) model, uses a simple approach that assumes that a nucleon colliding with a nucleus may be described in terms of scattering the incoming nucleon off the individual nuclear constituents. This model describes the overall features of high-energy scattering, such as the high energy of the forward-going particles, and qualitatively reproduces $d^2\sigma/dEd\Omega$ at energies above about 200 MeV and angles greater than 10 degrees [4]. In the INC calculation, energy is deposited in the struck nucleus. This energy is then dissipated by the evaporation of low energy particles. The evaporation model provides a reasonable description of cross-sections, but often does not get the correct ratio between the different kinds of emitted particles.

Consequently, the transport calculations performed using MCNP and the Los Alamos High Energy Transport code (LAHET) [8] are not completely accurate. It is generally believed that when they are used to determine average numbers, such as the total number of emitted neutrons or the total radioisotope production, one can expect errors of the order of ~20%. However, more specific details, such as the production of a specific radioisotope, may be in error by a much larger amount. It is therefore necessary to experimentally benchmark these calculations in a configuration resembling that to be used in the final construction. We have performed an experiment to measure the production of radioisotopes in stoppping-length W and Pb targets irradiated by a 800 MeV proton beam, and are comparing the results to values obtained from calculations using LAHET and MCNP. The experiment was designed to pay particular attention to the short half-life radionuclides, which have not been previously measured. In the following, we present details of the experiment, explain how we analyze the data and obtain the results, how we perform the calculations, and finally, how the experimental data agree with the calculations.

2. Experimental Method

The experiment was done using the "Target 2" external proton beam at the WNR (Weapons Neutron Research) facility at LAMPF. This area is fed by the H^- beam from the LAMPF linear accelerator at energies up to 800 MeV. A diagram of the WNR facility is shown in Figure 1.

Thick tungsten and lead targets were irradiated with 800 MeV protons. Thin foils were inserted at various locations to sample the radiation environment inside the target . The foils

were then removed and counted using high-resolution high-purity germanium gamma-ray detectors. The radioisotopes produced were then identified through their characteristic gamma-ray energy spectra.

The tungsten target, shown in Fig. 2, was 45.7 cm long and 20.3 cm square. A lead shield was placed on the front of the target to protect personnel from the high-activation region where the beam enters the target. Foils could be inserted at 5-cm intervals from the front of the target. Fig. 3a. shows a diagram of the Pb target. Foils were held in a lexan polycarbonate holder, similar to the Pb foil holder shown in Fig. 3b. The foils inserted on the beam axis were to measure interactions due primarily to the incident beam; the off-axis foils sampled interactions due to scattered and secondary particles (primarily neutrons.) The foils were 0.191 cm (0.750 in) diameter disks, with nominal thickness of either 0.051 cm (0.020 in) or 0.102 cm (0.040 in.)

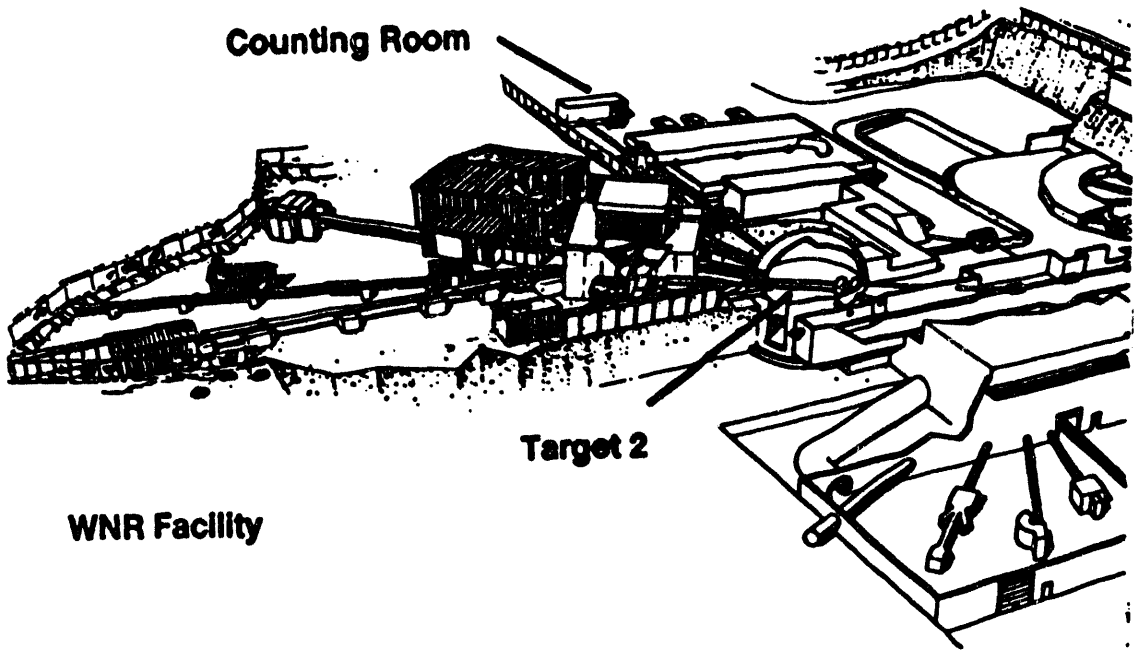

Fig. 1. The WNR Facility at LAMPF. Beam is delivered from the LINAC off the page to the right. Target 2 and the counting room for this experiment are indicated.

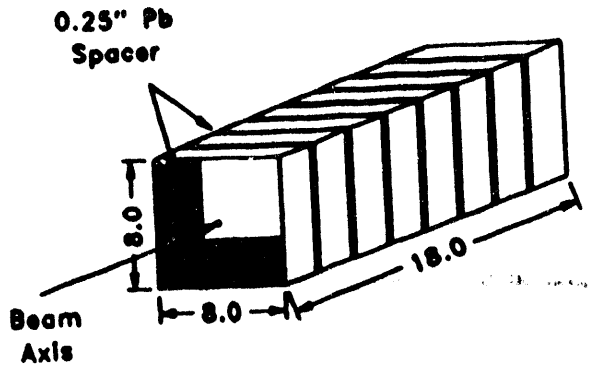

Fig 2. Drawing of the Tungsten target. Dimensions in inches.

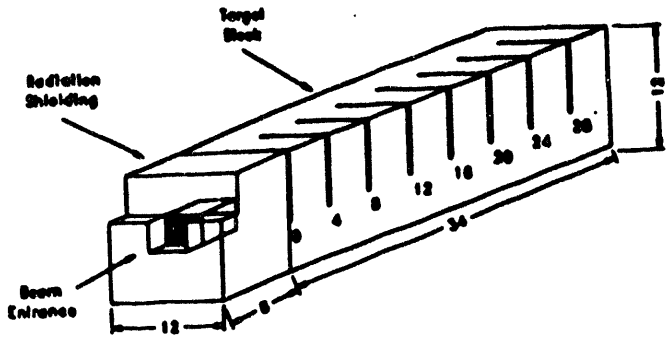

Fig 3a. Lead target. Dimensions are in inches.

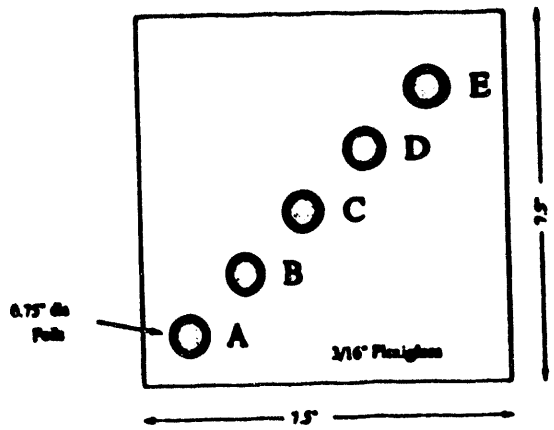

Fig. 3b. Lead target holder.

Irradiation times varied from a few seconds up to 8 hours, to study short-lived and long-lived isotopes respectively. This experiment represents the first study of short-lived thick-target W spallation products. Fourteen short irradiations, 1 one-hour, and 1 eight-hour tungsten irradiation were made. The W irradiations are summarized in Table 1. The proton beam fluence was determined by activation of thin aluminum foils. These foils were 0.00686 g/cm^2 for the 8 hr run, and 0.217 g/cm^2 for the shorter runs. Gamma rays from the decay of ^{24}Na produced in the ^{27}Al(p,3pn)^{24}Na were counted, and the absolute number of protons calculated using a value for the cross section of 10.94 ± 0.24 mb/sr [9]. Table 2 summarizes the Pb irradiations, but only shows an estimated proton fluence based on the average number of protons per beam micropulse, 3 x 10^8. The Al activation for the Pb runs has not yet been analyzed.

Table 1. Tungsten Irradiation Times

Run No.	Beam Pulses	Time (Sec)	Total number of protons
189	2,055	7	$8.33 \pm 0.65 \times 10^{11}$
191	3,000	10	$1.10 \pm 0.06 \times 10^{12}$
193	6,000	98	$2.53 \pm 0.09 \times 10^{12}$
195	20,000		
197	3,000	3	$9.17 \pm 0.57 \times 10^{11}$
199	5,000	6	$1.65 \pm 0.09 \times 10^{12}$
201	10,000	12	$3.01 \pm 0.10 \times 10^{12}$
206	20,000	31	$8.33 \pm 0.65 \times 10^{11}$
208	40,000	63	
210	80,000	125	$2.25 \pm 0.02 \times 10^{13}$
212	100,000	156	$2.18 \pm 0.05 \times 10^{13}$
214	1,150,081	3907	$3.31 \pm 0.01 \times 10^{14}$
214	4,309,096	21945	$2.58 \pm 0.04 \times 10^{15}$

Table 2. Lead Irradiation Times

Run No.	Beam Pulses	Time (Sec)	Estimated Total Protons
134	2,000	3	6.0×10^{11}
137	2,000	3	6.0×10^{11}
151	2,000	4	6.0×10^{11}
153	5,000	9	1.5×10^{12}
156	10,000	19	3.0×10^{12}
158	20,000	36	6.0×10^{12}
160	40,000	71	1.2×10^{13}
162	80,000	146	2.4×10^{13}
164	200,000	367	6.0×10^{13}
168	1,000,000	1352	3.0×10^{14}
182	5,453,113	4265	1.6×10^{15}

A germanium-detector counting system was set up at the WNR so that the short-irradiation foils could be counted immediately for information on short-lived radioisotopes. A procedure was developed so that target foils could be removed from the target and placed on the counters in about five minutes. Five Ge detector systems were set up in a CAMAC-based data acquisition system using the acquisition program XSYS. A diagram of the associated electronics is shown in Fig. 4. The electronics was designed to gate the proton beam on for a preset number of pulses, wait a predetermined interval, and then gate the ADC's on and off for a number of counting intervals. Typically, the waiting interval between beam off and the first count was set to be 5.00 minutes, and fifteen counts of 3.00 minutes each were taken. From this series of counts, the half-life of the radionuclides could be determined. The electronics was designed to allow individual counting intervals for each detector, but this feautre was not used. The system also counted the number of beam pulses, measured the exact start and stop time of each count, and determined the deadtime of the system.

The foils from the one-hour runs were first counted at the WNR, and then transported to the automated counting facility of the Isotope and Nuclear Chemistry (INC) Division. All of the foils from the eight-hour irradiations were counted at INC. These counts were made for up to 35 days after end of bombardment and were counted for longer periods of time, typically 50 to 100 minutes each.

The detectors were calibrated for energy and detector efficiency using a commercial standard source traceable to NIST [10]. However, the thick foils used in the irradiation transmitted only about 10% of the lower energy gamma rays, making a precise determination of the product of efficiency and transmission very important. This was calculated using the computer code EFFIC [11], which was verified against the standard source. A typical efficiency curve for several foil thicknesses on WNR detector five is shown in Figure 5.

APT ELECTRONICS DIAGRAM

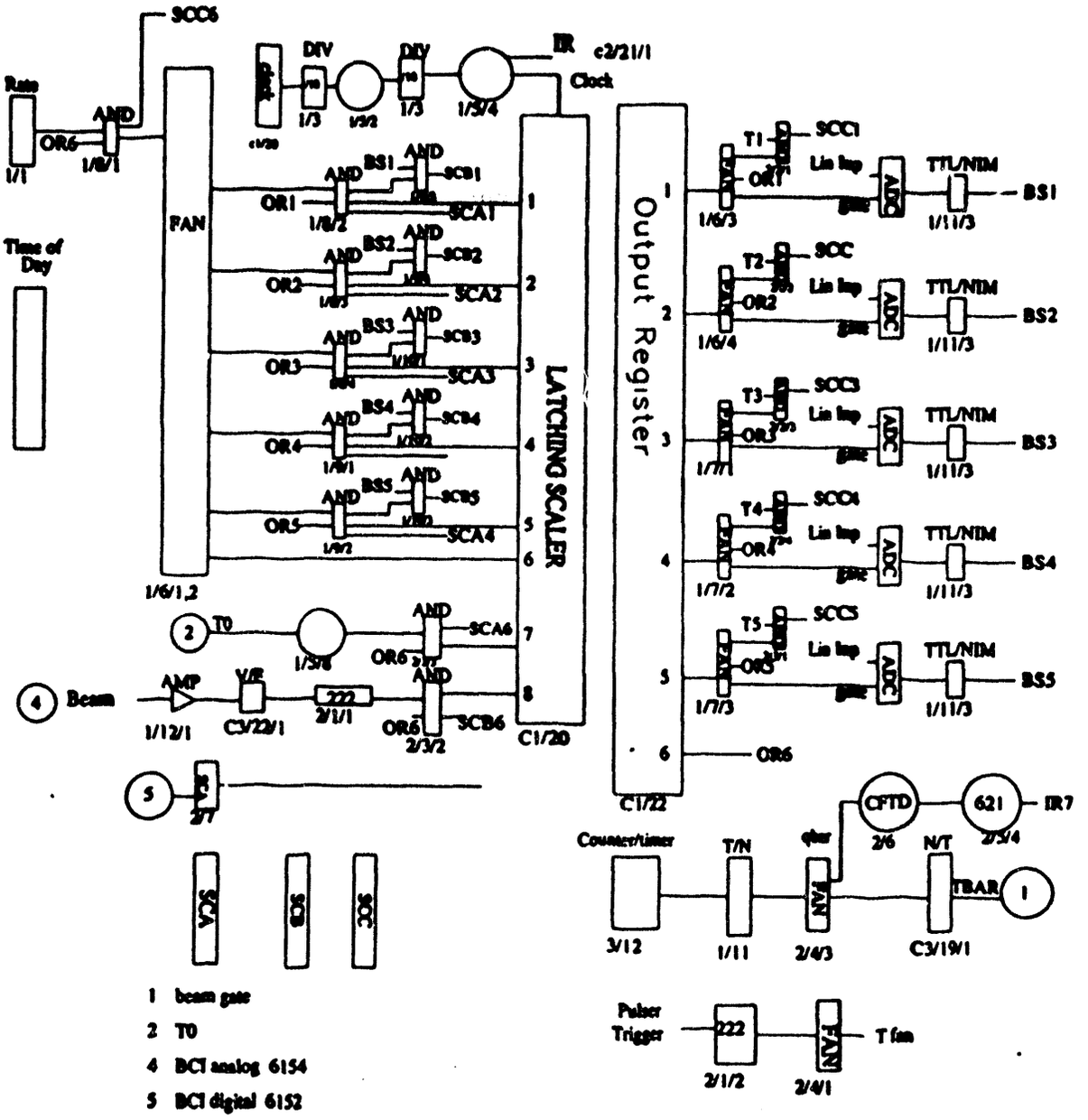

Fig. 4. Electronics diagram for APT Experiment.

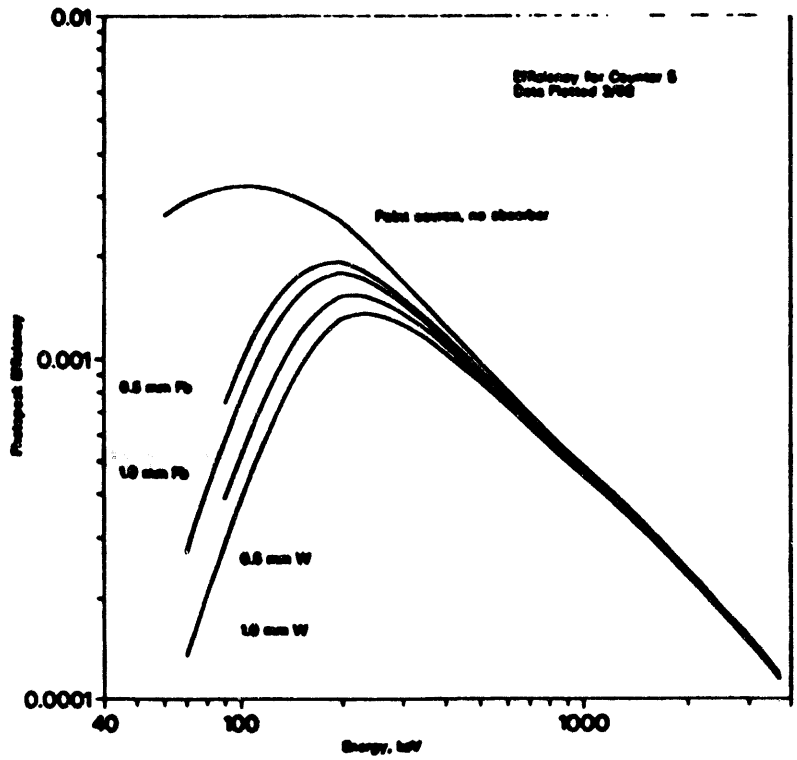

Fig. 5. Calculated efficiency curve for WNR Detector 5. The efficiency for various thickness foils is shown.

Approximately 2500 spectra were obtained from the short half-life runs, each containing approximately 100 analyzable peaks. About five-hundred spectra were measured at longer times, each containing 200 to 300 peaks. Gamma peak areas were determined by the automated peak-fitting code GAMANAL [12]. This code internally optimizes the energy calibration, peak shape parameters and background using known peaks in the measured spectrum. The energy determination was accurate typically to less than 1 keV. Radionuclide identification was suggested by GAMANAL based on a gamma-ray library, and then checked against half-life. The internal gamma-ray library was updated to include candidate spallation-product nuclei using the tabulation of Spanier and Ekstrom [13], which was based on the ENDF compilation of March 8, 1989.

Sample gamma-ray spectra from the one hour W irradiation are shown in Fig. 6. The spectra are from a tungsten foil in position 4A, and are shown after several decay times. It is interesting to note several regions of the spectrum. The peak at about channel 600 (300 kev) has about the same strength at all times, indicating a very long half life. The peaks near channel 2000 (approx. 1000 keV) show more structure at long decay times, perhaps indicating parent-daughter buildup, while the peaks near channel 3500 (approx 1750 keV) die away at longer times, indicating decay.

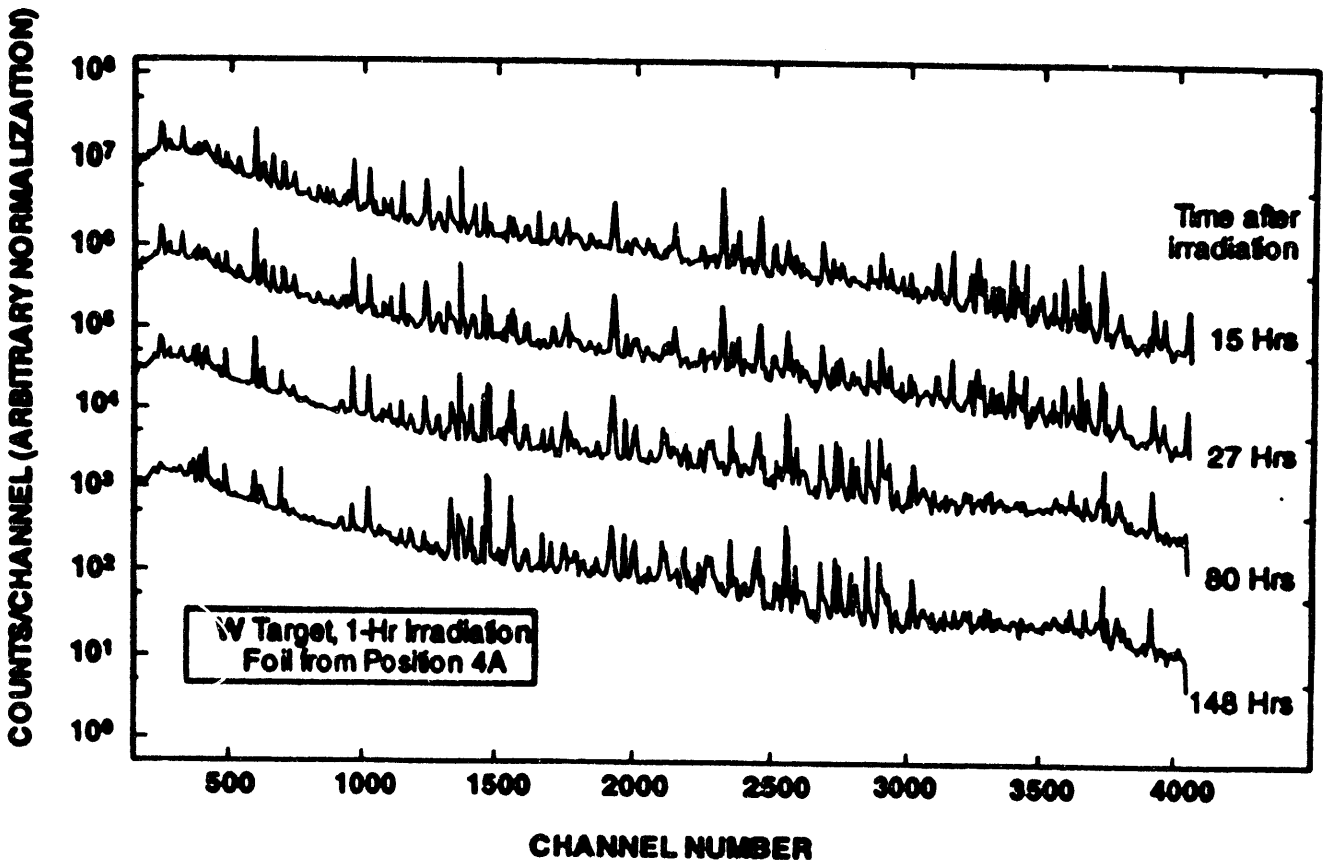

Fig. 6. Several W spectra at different decay times from foil 614, taken using the INC counting facility. The approximate energy calibration is 0.5 keV/channel.

3. Model Calculations

Initially we consider scoping calculations in a simple geometry, a tungsten cylinder 40 cm long and 20 cm radius. These calculations demonstrate the properties of spallation with 800 MeV protons, and subsequent transport and interactions of the secondary particles. One measure of the distribution of particles is the energy deposited by them in individual volume elements. Figure 7 depicts the energy deposited per unit mass (MeV/g) due to the high-energy particles (primary beam and all secondaries, except neutrons below 20 MeV) as

calculated by LAHET. We note that most of the energy deposition is concentrated in the first ~15 cm depth and ~5 cm radius, with extended tails out to longer distances and larger radii. The energy deposition due to low-energy neutron induced reactions, calculated using MCNP, is presented in Fig. 8. These low energy neutrons ($E \leq 20$ MeV) have a long mean-free-path (average distance between interactions) and spread around over much larger volumes. They are the primary source of activation products far from the beam axis, and deep inside the cylinder. These neutrons are the basis for the APT and ATW projects, where their high fluxes are utilized for tritium production and waste transmutation.

Figure 9 depicts the mass distribution of spallation products 2 cm deep inside the cylinder, as a function of the radius. Close to the beam, the mass yield contains many low-mass products, which result from a large number of particles removed from the target nucleus. This implies that the nucleus was hit by a high-energy particle, which had the energy to remove a lot of mass. At larger radii, the mass distribution is much narrower, since the particles at these radii have much less energy, and consequently cannot remove as many particles from the target nucleus. Figure 10 shows the mass distribution as one goes deeper into the cylinder on the beam axis. Again, the mass distribution becomes narrower as the penetration goes deeper because the primary beam loses much of its energy, and the number of secondary, lower-energy particles increases. A different aspect of these processes is seen in Fig. 11. Here we compare mass yields from interactions of the primary beam to the total mass yield (from all particles) as a function of mass. Masses around that of tungsten evidently sample mainly secondary particles (their low energy causes emission of a very few particles), whereas masses around 160 sample the primary beam almost exclusively. Consequently, studying mass yields provides a large amount of information on the various physical processes. Deep inside the cylinder as well as at large radii, we are sampling spallation from secondary products and neutron activation. Near the beam center, we can study spallation due to both the primary beam and secondary particles using the mass distribution to discriminate between the different types of particles.

In the calculations used for comparison to the experimental data, the entire tungsten stack, lead shield, lexan holders, and foils were coded into LAHET and MCNP using their exact dimensions, with one exception: The tungsten foils themselves were assumed to have a 0.223 cm thickness and a 2.064 cm diameter, equal to the dimensions of the hole in the foil holder. This was done to increase the statistics of sampling by the simulation codes, in order to minimize statistical errors. It is not expected to cause any systematic error to the calculational results.

The full calculation ran 300,000 events of 800 MeV protons using LAHET. Neutrons from these events with energies below 20 MeV were written to a "NEUTP" file, and subsequently read and processed by MCNP. A listing of the input files for the LAHET and MCNP calculations is in Appendix A. The neutron flux produced in MCNP is used by CINDER'90 [14] to obtain a table of neutron activation products. The table of primary isotopes produced in spallation reactions was obtained from the LAHET "HISTP" file. These isotopes are then

transmuted using CINDER'90, which produces tables of activities of specific foils, broken down into the different isotopes producing the activity. This was done for different irradiation and different decay times, matching the irradiation and decay times in the experiment.

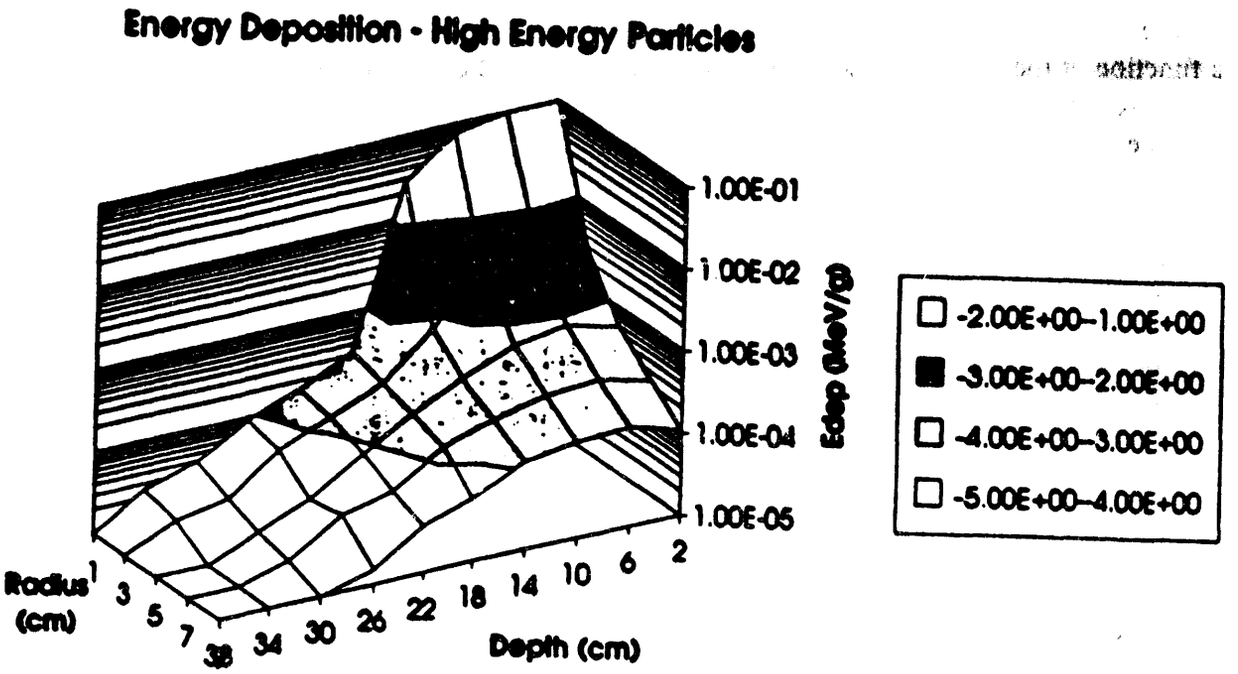

Fig. 7. Energy deposition as a function of radial position and depth in the cylinder. The legend indicates the power of 10 of the energy deposition.

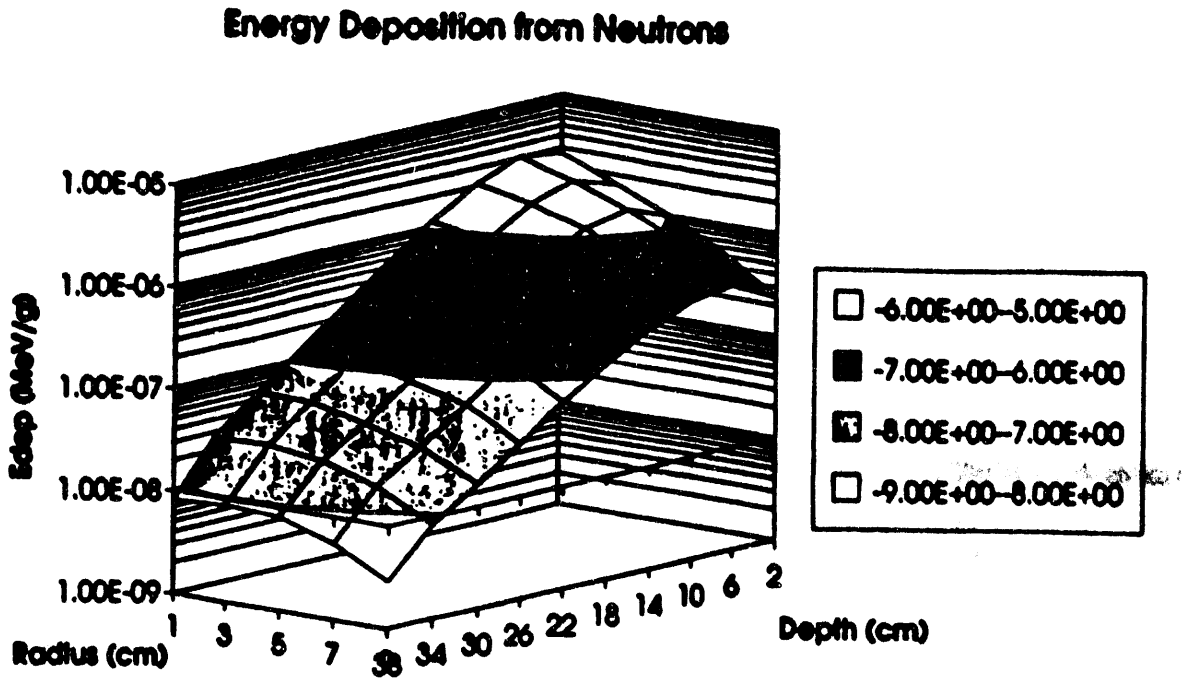

Fig. 8. Energy deposition from low- energy (<20 MeV) neutron-induced reactions, as a function of radial position and depth in the cylinder. The legend indicates the power of 10 of the energy deposition.

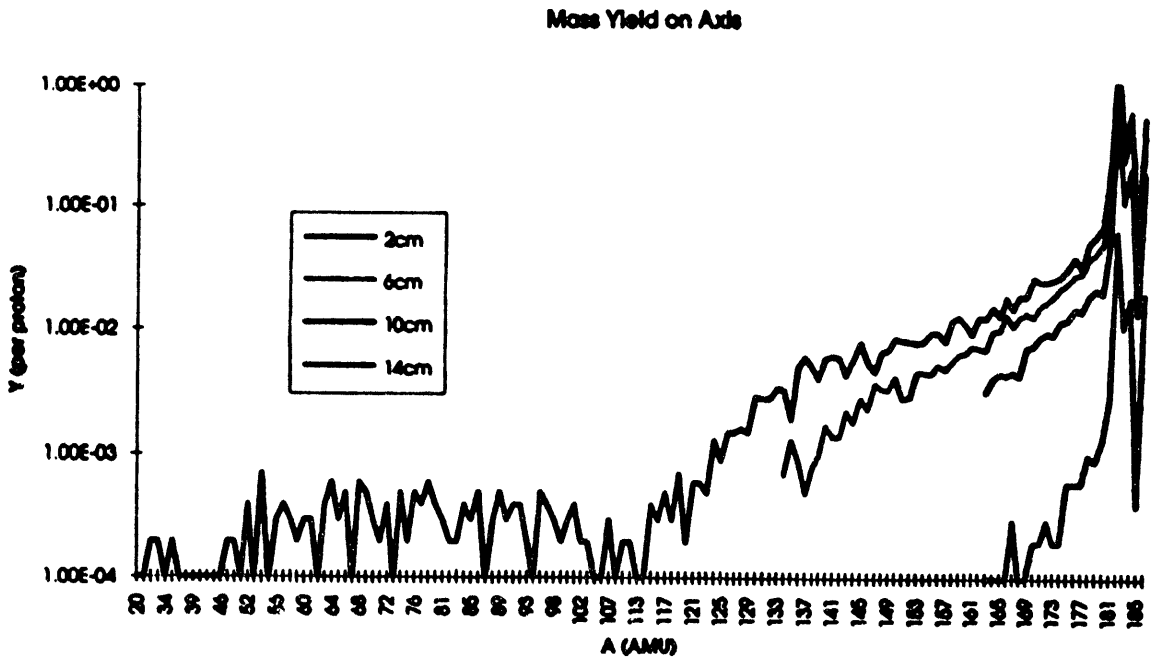

Fig. 9. Yield (as function of mass) of spallation products for different radii, at 2 cm depth in the cylinder. The top curve is for 2 cm radius, the bottom for 14 cm radius.

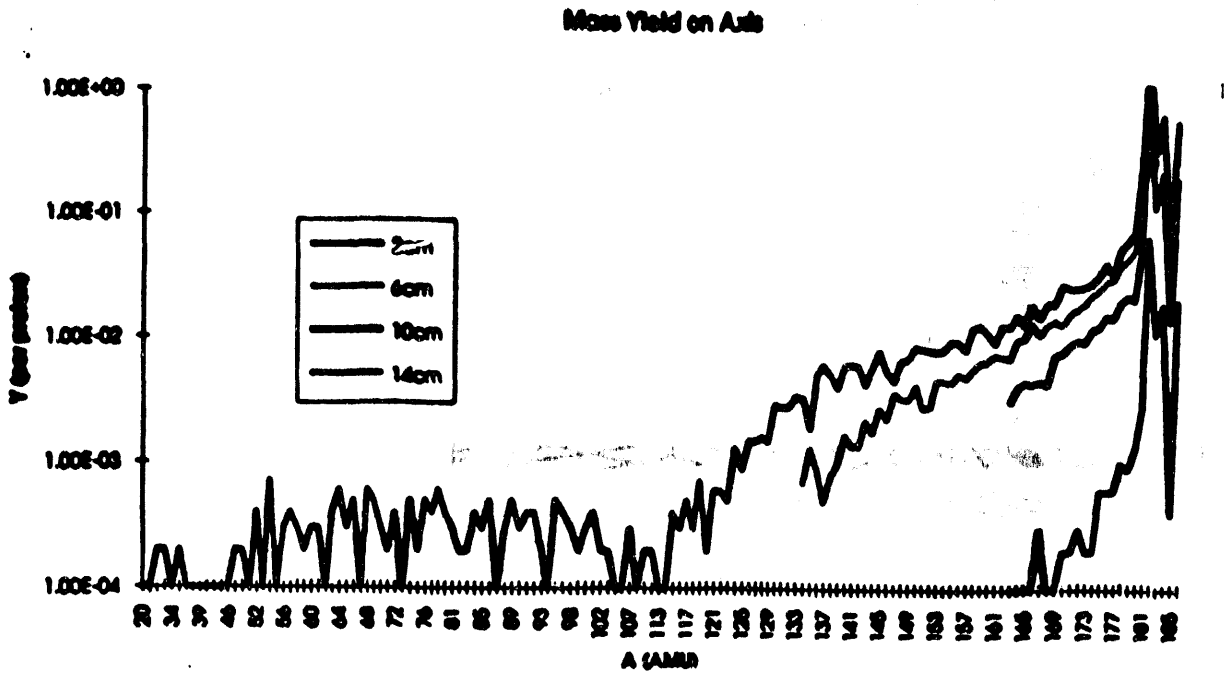

Fig. 10. Spallation mass yield on the beam axis, at different depths into the cylinder. The top curve is for 1 cm depth, the bottom for 7 cm depth.

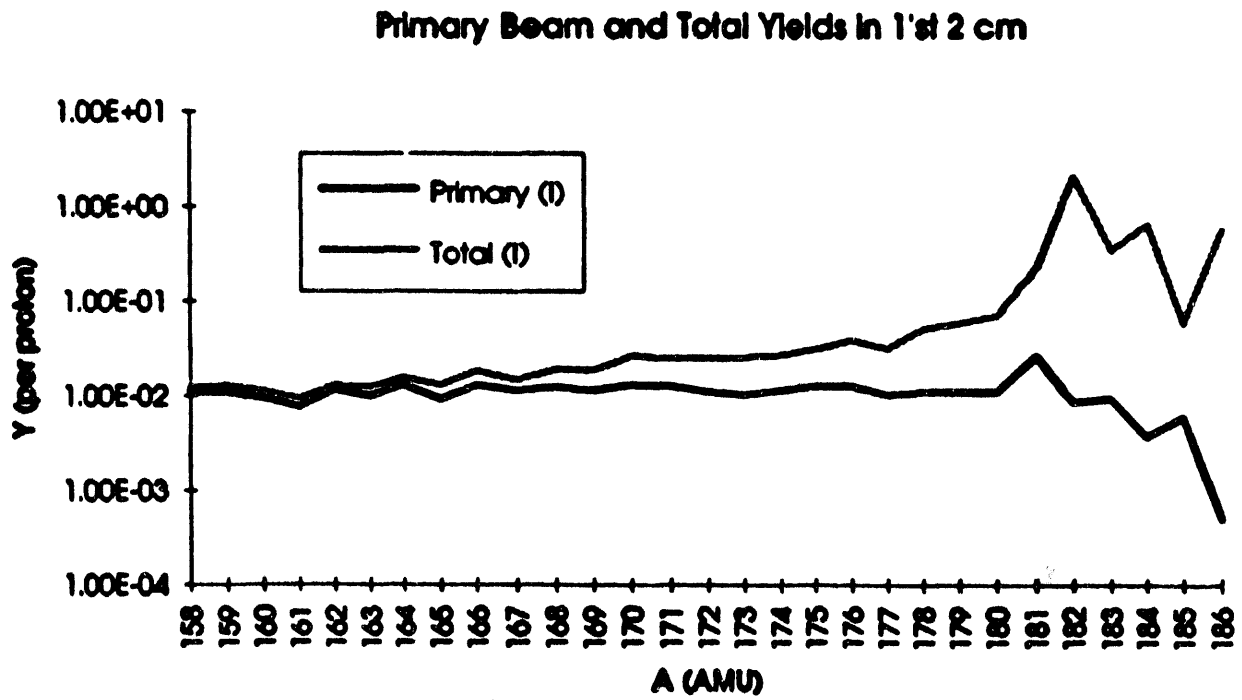

Fig. 11 On-axis mass yields from all reactions and from primary beam spallation only at 2 cm depth in cylinder.

4. Analysis

A very large set of data was collected, and the analysis, even though partially automated, was still very labor-intensive. For this reason, it was decided to begin the analysis with the W data, since W is an important element in the Los Alamos APT design and no thick-target spallation product data on W exists. A large amount of preliminary work was needed before spallation product yields could be determined. This work included determining an accurate energy and efficiency calibration for each detector, adapting the GAMANAL peak-fitting code to handle XSYS-generated data and correct for small but non-trivial nonlinearities in the WNR data-collection system, and updating the radionuclide library to include current data on medium-mass nuclei. The analysis reported here includes all the on-axis (Position "A") W foils, and the off-axis foil at radius 3.0 cm (Position "B") at 10 and 20 cm (4 and 8 in) from the front face of the target.

Figure 12 shows a gamma-ray spectrum from the 1 hour irradiation, 140 hours after end of bombardment. Identified gamma rays are marked.. Many observed gamma lines have unresolved contributions from several different nuclei.. The results presented here depend primarily on gamma peaks with a unique decay scheme where possible, and on two-component gamma peaks which can be time-resolved into their individual decays. In addition, many of the nuclei calculated to be produced have decay schemes unfavorable for detection. These nuclei may have extremely short half lives, decay schemes that involve below-threshold gamma rays, or peaks to which more than two nuclei contribute.. Thus a comparison must be made only between observed and calculated yields. In most cases, an unobserved yield did not neccessarily imply that the nucleus was not produced.

The data were analyzed in two ways. First, in order to compare to the large body of thin-target spallation data, we attempted to extract raw spallation yields. This was done by first identifying nuclei by their gamma ray energies and half life, and then extrapolating their decay back to end of bombardment. A set of computer codes were written to start this analysis. These codes scanned the gamma ray tables, did one- and two- component decay fits, and provided a preliminary identification of the radionuclides. All nuclei with a given mass were then analyzed for parent-daughter buildup. A computer code PARENT was written to estimate the daughter yield in the presence of up to three parents. The normal textbook parent-daughter decay formulas do not include the contribution of several parents at zero time, and the necessary formulae that were derived are presented in Appendix XX.

Figure 13 shows two sample parent-daughter corrections. Fig. 13A illustrates the effect of a single parent on the decay curve of the daughter. Fig. 13B shows how multiple parents can contribute. In many cases, the parent nuclei were calculated to be present, but because of unfavorable decay schemes or very short half-lives could not be observed. The yields of the daughter nuclei in these mass chains could not be corrected, and are presented as cumulative yields, that is, the observed nucleus represents the sum of spallation production and parent decay. The data presented as independent yields have either been corrected for parent contributions, have parents that are observable but were not observed and were also

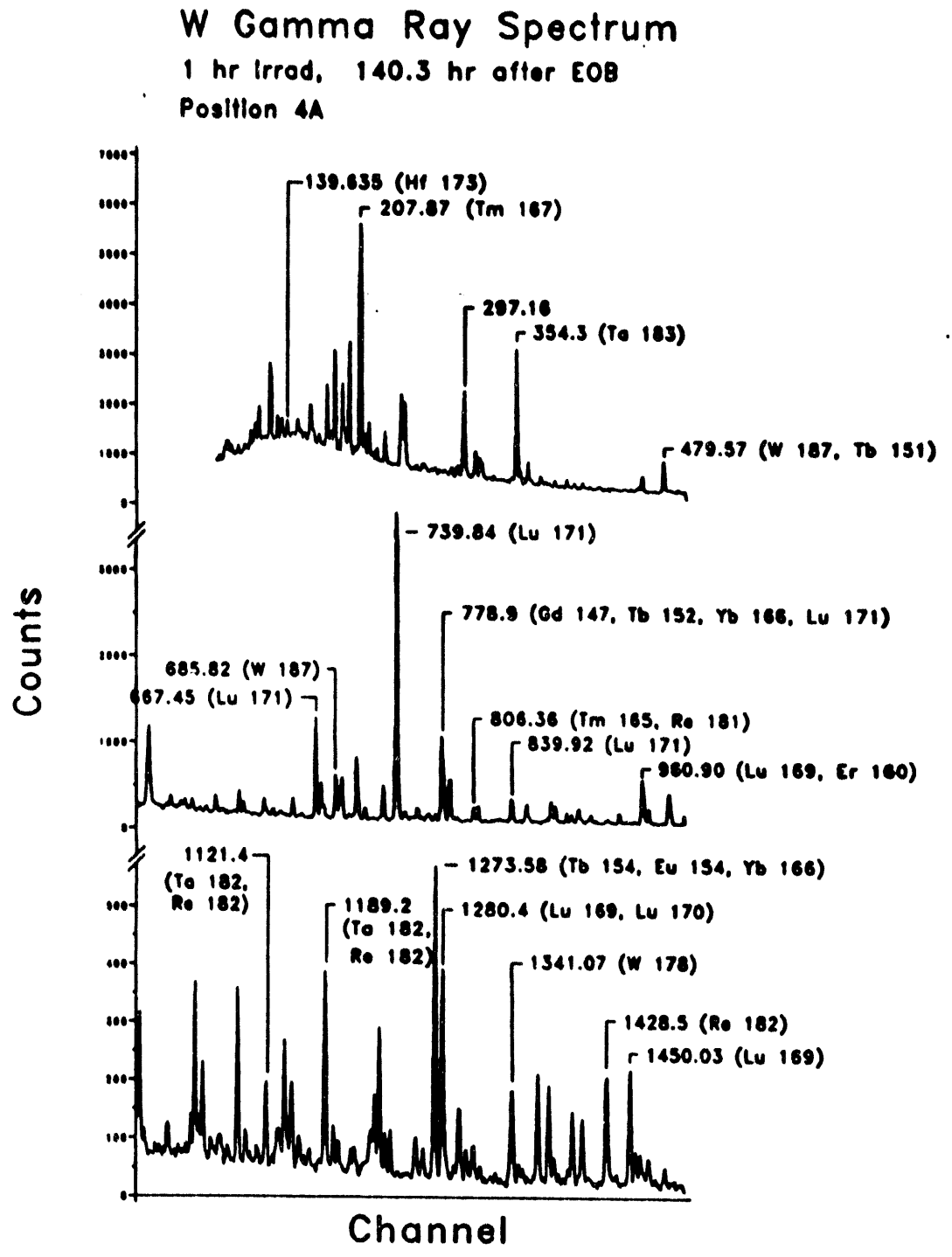

Fig 12. Tungsten gamma ray spectrum from on-axis position 4A (Foil 614) 140 hours after end of 1 hr bombardment.

calculated to be small, or were truly independent by virtue of having a stable or long-lived parent.

The Lahet calculations give spallation yields independent of the duration of bombardment. Therefore the measured yields at end-of-bombardment were corrected for decay during production by the relation:

$$R = \frac{\lambda\, n(t)}{1 - e^{-\lambda t}}$$

where n(t) is the number of nuclei present at time t, λ is the decay constant, and R is the production rate. The half-lives of observed nuclei were typically long compared to the bombardment time and in most cases this correction was less than 1%.

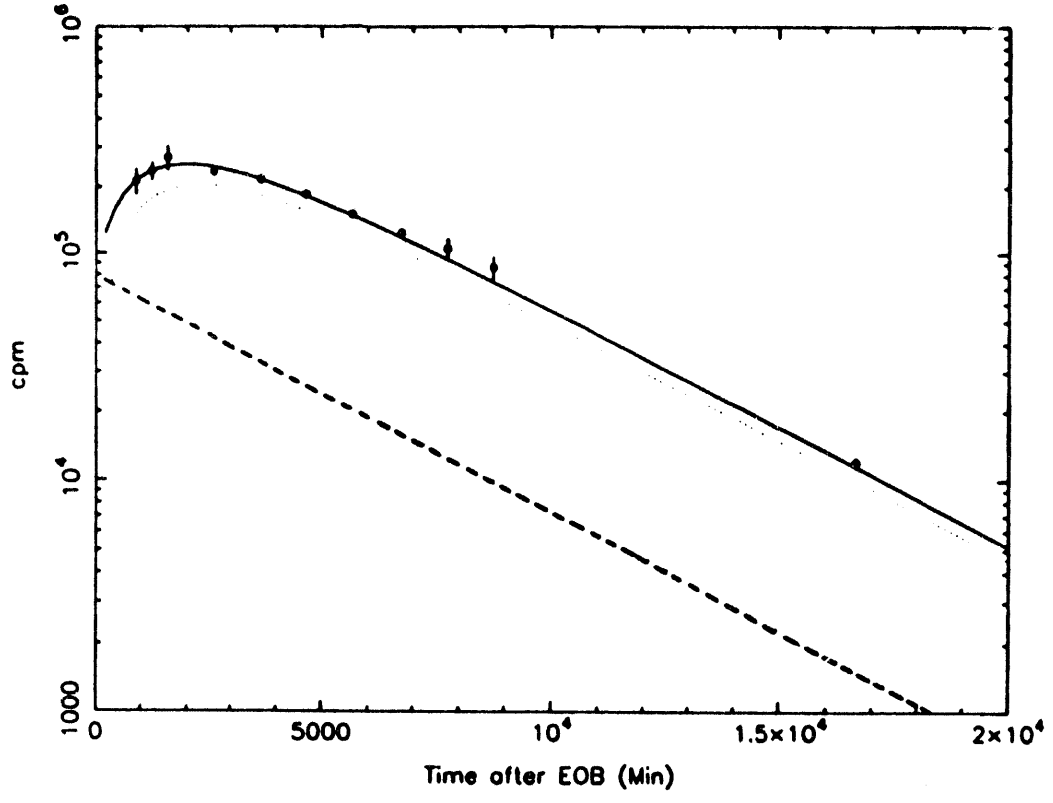

Figure 13A. Parent correction to the decay of the 985.1 keV line of ^{170}Lu. The dotted line indicates the contribution from ^{170}Hf ($T_{1/2}$=16 h), the dashed line is the fitted contribution from ^{170}Lu ($T_{1/2}$=2.02d). The sum of the two is shown as the solid line.

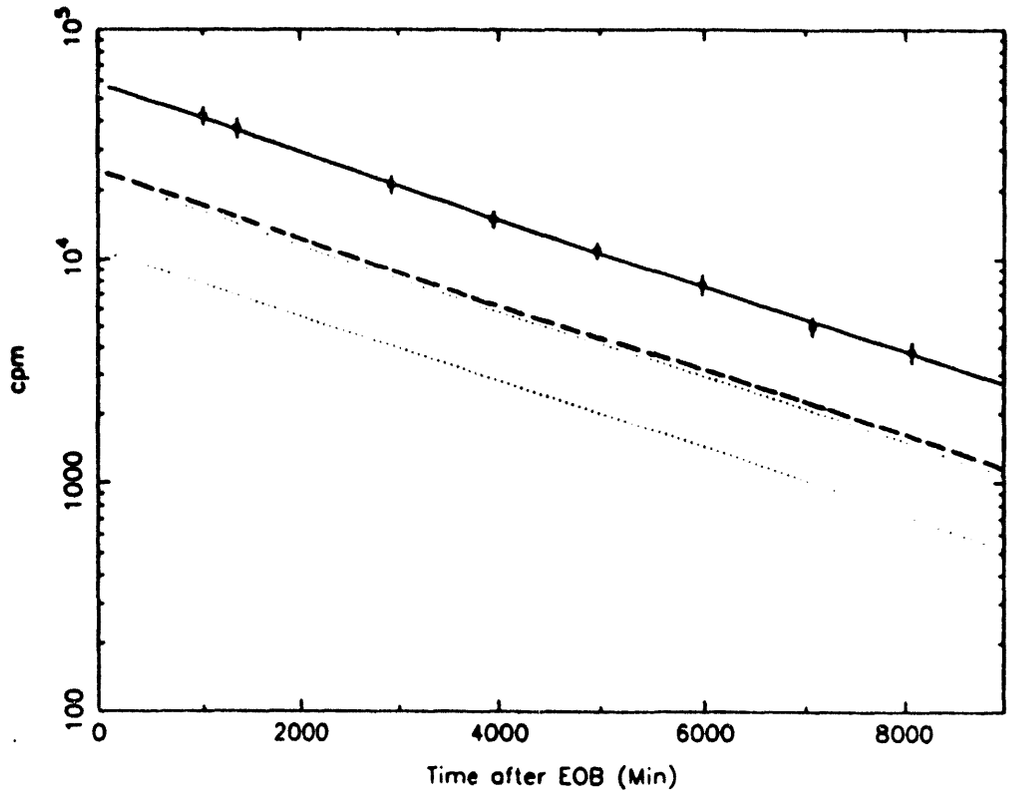

Fig 13B. Multiple parent correction to the decay of ^{169}Lu. The dotted lines indicate the measured contributions from ^{169}Ta (4.90 m) and ^{169}Hf (3.25 m). The dashed line is the fit contribution from ^{169}Lu (1.42 d).

The second comparison was made directly to the CINDER-90 calculations, which were done at the exact times at which measurements were made. CINDER-90 starts from the calculated spallation yield and low-energy (< 20 MeV) neutron flux, and calculates decay during production, parent decays, and low-energy neutron capture reactions. A code CPLOT was written to display the calculations and the decay data for chosen gamma ray energies. CPLOT would scan the gamma ray table for all nuclei with gamma ray energies within detector resolution of the specified energy and fold the tabulated branching ratios with the calculated number of nuclei at each time calculated. The most abundant four nuclides were displayed. The sum of the four most abundant nuclei was fit to the data, producing an overall normalization factor. The gamma peaks often had contributions from several nuclei, and no direct comparison of data and calculation could be made in those cases. Where only a single nucleus contributed to a given peak, a ratio of data to calculation could be extracted. This ratio was calculated by CPLOT.

Samples of CPLOT output are shown in Figure 14. Fig. 14A shows an example of an excellent fit to the 427.0 KeV line of ^{177}W. (The ^{178}Ta contribution, with a half-life of 9.3 m, was negligible.). The calculation required a normalization of 1.71, and with this factor the χ^2/n was 0.2. Fig 14B shows a case in which three nuclei are calculated to contribute about equally to the 137. keV peak, and no information on an individual nucleus can be obtained.

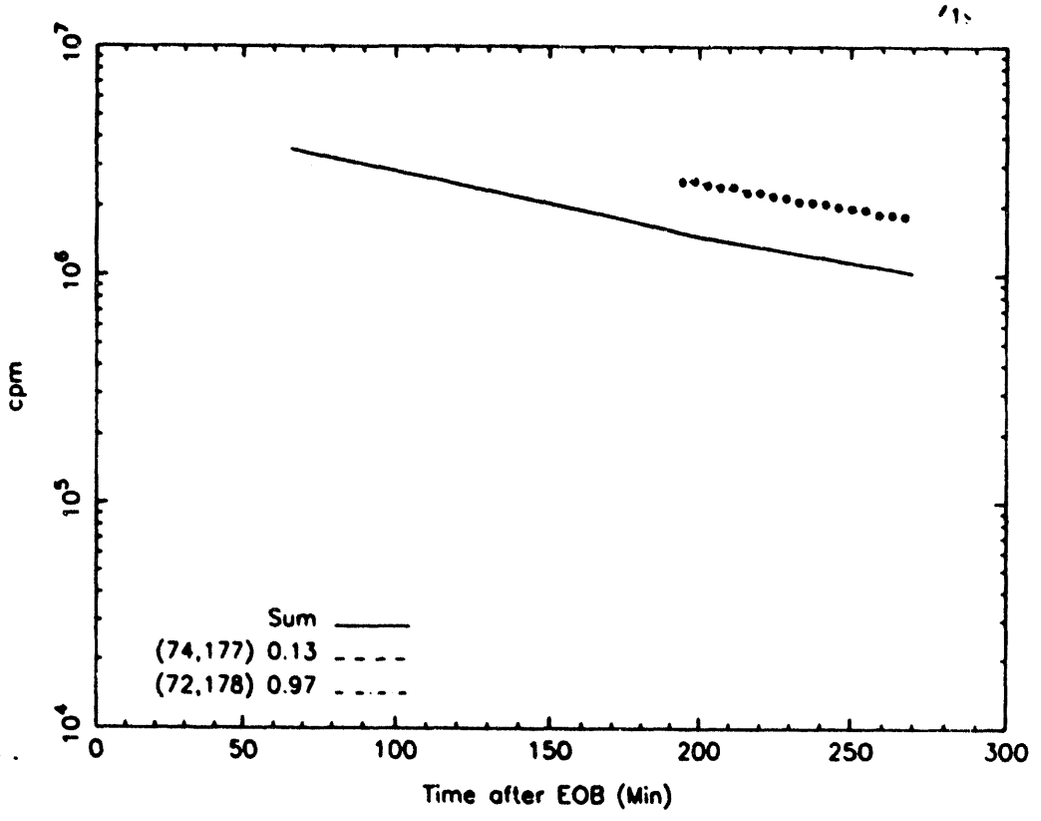

Figure 14A. Comparison of CINDER'90 calculation with data for 427. keV peak. The contribution of ^{178}Ta is negligible. The renormalization factor was 1.71. The fit of the renormalized curve to the data (shown by a dotted line through the points) had a χ^2/n of 0.2,

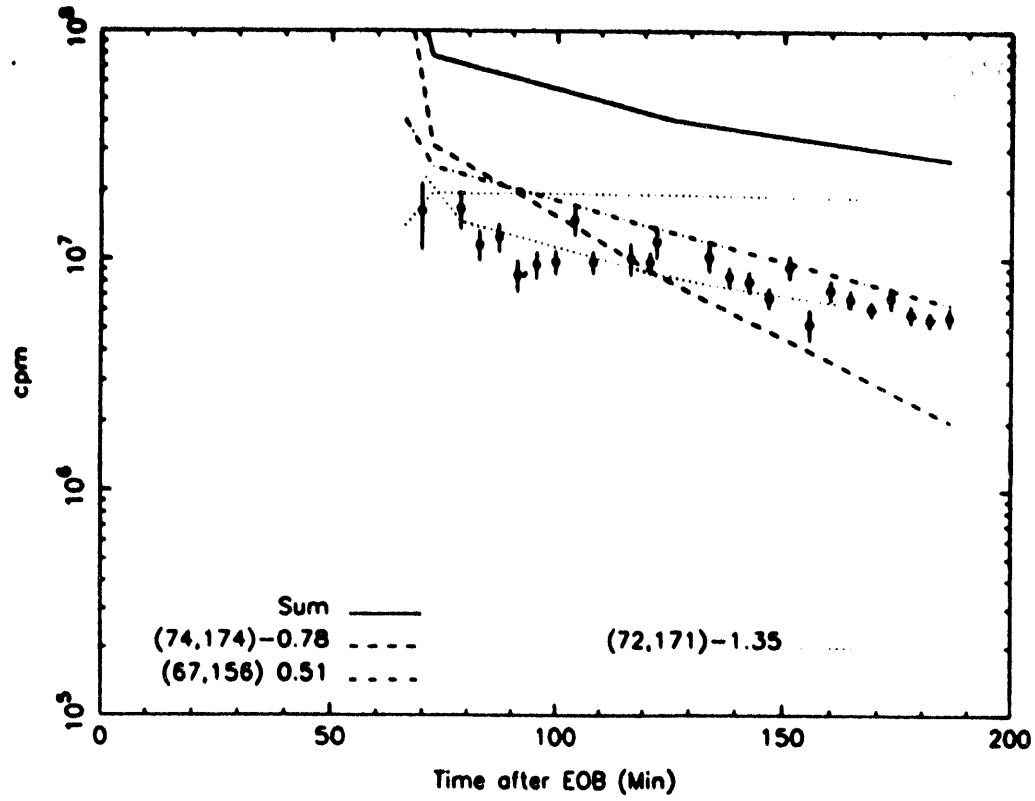

Fig. 14B. CINDER'90 calculation for 137. keV compared to data. Several nuclei contribute about equally, and no information on an individual nucleus can be extracted.

5. Results

5a. General Results

The extracted yields, in nuclei/cm^3/proton, are listed in Table 3 These are the combined results of the analysis of the short, one hour, and eight-hour irradiations. (Only the one-hour irradiation was analyzed for position 2A.) It should be noted that the yields are averaged over the entire volume of the activated foil. For foils near the front of the target the area of the beam may be less than the foil area. As noted earlier, nuclei may have been produced, for which yields could not be obtained due to unfavorable decay schemes, very short half-lives, etc. The absence of a nucleus does not necessarily indicate that it was not produced, only that it could not be measured reliably. Table 3 also shows the ratio of the measured yields to the LAHET and CINDER'90 calculations.

Table 3A Tungsten Spallation Yields for Position 2A

Z	Sym	A	Independent Yield n/cc/p	"+/-"	Cumulative Yield n/cc/p	"+/-"	Calculated (LAHET)	Ratio LAHET	Ratio CINDER'90
54	Xe	121	8.62E-03	1.29E-04			0		
52	Te	121			5.25E-04	4.27E-05	0		
54	Xe	123	4.68E-03	1.16E-04			0		
53	I	126			3.55E-03	6.69E-05	0		
54	Xe	131			9.47E-03	1.97E-03	0		
53	I	132	1.36E-03	2.05E-04			0		
52	Te	132			1.05E-03	2.84E-04	0		
58	Ce	133			3.10E-03	2.42E-03	1.75E-04	17.7	
56	Ba	133			2.75E-04	4.14E-05	0		
56	Ba	135			7.96E-04	3.93E-05	0		
63	Eu	145			8.49E-04	3.83E-05	8.28E-04	1.025	
63	Eu	146	1.75E-04	3.48E-06			1.22E-03	0.143	
64	Gd	146	6.51E-04	6.53E-05			9.58E-04	0.68	
65	Tb	147	3.66E-04	3.56E-04			4.36E-04	0.839	0.61
64	Gd	147	1.25E-03	2.88E-05			1.13E-03	1.106	
63	Eu	147	5.47E-03	5.22E-05			5.67E-04	9.647	
65	Tb	149	1.30E-03	1.18E-05			9.15E-04	1.421	
64	Gd	149	2.91E-04	5.44E-06			7.84E-04	0.371	
60	Nd	149	1.28E-03	9.18E-05			0		
65	Tb	150			3.22E-04	1.51E-05	1.18E-03	0.273	3.883
65	Tb	151			1.40E-03	2.11E-05	6.10E-04	2.295	2.23
65	Tb	152	1.05E-03	1.05E-05			6.54E-04	1.606	0.314
66	Dy	152	6.67E-04	7.52E-06			1.44E-03	0.463	0.305
66	Dy	153	4.17E-05	6.34E-06			9.58E-04	0.044	
65	Tb	153	2.08E-03	1.67E-05			3.04E-04	6.842	
65	Tb	155	2.76E-03	2.11E-04			1.31E-04	21.069	
66	Dy	155	1.53E-05	1.66E-07			4.79E-04	0.032	0.538
67	Ho	155	2.10E-03	5.25E-04			1.13E-03	1.858	
62	Sm	156	7.52E-03	2.35E-04			0.00E+01		
67	Ho	156	1.33E-03	3.42E-05			1.05E-03	1.267	1.371
66	Dy	157			3.09E-03	1.69E-04	1.31E-04	23.588	1.315
67	Ho	159	5.86E-03	8.97E-04			2.18E-04	26.881	0.792
67	Ho	160	1.33E-03	3.18E-04			1.75E-04	7.6	
68	Er	160			7.90E-03	3.95E-04	1.05E-03	7.524	
68	Er	161			3.99E-03	3.36E-04	2.61E-04	15.287	1.052
69	Tm	162	7.95E-04	9.73E-05			1.09E-03	0.73	1.809
69	Tm	163			3.58E-03	7.17E-05	1.09E-03	3.284	0.859
69	Tm	165			4.41E-03	1.33E-04	3.93E-04	11.221	1.609
70	Yb	166			6.30E-03	1.58E-03	1.05E-03	6	
69	Tm	166	2.54E-04	2.79E-06			1.75E-04	1.451	12.074
71	Lu	169			5.46E-03	3.15E-05	1.48E-03	3.689	2.872
70	Yb	169	1.62ee-4	7.96E-06			4.36E-05	37.156	
72	Hf	170	5.78E-03	2.21E-05			2.40E-03	2.408	0.748
71	Lu	170	4.87E-04	3.76E-06			6.54E-04	0.745	
72	Hf	171	5.10E-03	3.37E-05			1.13E-03	4.513	
71	Lu	171	2.67E-03	7.80E-06			6.10E-04	4.377	
68	Er	171	1.61E-04	3.64E-06			0		
72	Hf	172			4.20E-03	1.47E-03	1.44E-03	2.917	

71	Lu	172	6.89E-04	5.95E-06	3.93E-04	1.753	
73	Ta	173	4.20E-03	7.81E-05	3.91E-03	1.317	1.271
72	Hf	173	3.89E-03	2.50E-05	4.79E-04	8.121	0.653
74	W	174	3.57E-03	4.84E-04	3.09E-03	1.155	0.558
73	Ta	174	5.28E-03	6.33E-05	2.83E-03	1.866	0.809
73	Ta	175	5.28E-03	6.33E-05	2.44E-03	2.164	1.876
73	Ta	176	1.41E-03	1.04E-05	2.71E-03	0.521	1.018
74	W	176	5.25E-03	1.31E-03	4.31E-03	1.218	
74	W	177	4.09E-03	7.67E-05	3.65E-03	1.121	0.849
74	W*	178	8.82E-05	2.03E-05	6.82E-03	0.014	0.012
73	Ta	178	1.90E-03	1.74E-05	2.23E-03	0.852	
75	Re	181	4.23E-03	5.67E-05	1.62E-03	2.611	0.092
75	Re	182	6.07E-03	2.21E-04	7.40E-04	8.203	10.341
73	Ta	183	1.74E-03	3.64E-05	3.22E-03	0.54	
75	Re	184	8.24E-04	4.96E-05	3.04E-04	2.711	
73	Ta	184	2.91E-04	4.35E-06	9.15E-04	0.318	0.357
72	Hf	184	2.52E-04	6.30E-05	4.36E-05	5.78	
72	Ta	185	2.44E-03	6.83E-04	1.75E-03	1.394	1.126
74	W	187	5.63E-03	4.22E-05			0.483

Table 3B Tungsten Spallation Yields for Position 4A

Z	Sym	A	Independent Yield n/cc/p	"+/-"	Cumulative Yield n/cc/p	"+/-"	Calculated (LAHET)	Ratio LAHET	Ratio CINDER'90
65	Tb	151	1.15E-04	3.56E-06			3.93E-04	0.293	0.616
65	Tb	153	2.33E-04	6.09E-06			2.61E-04	0.892	
65	Tb	155	6.70E-05	2.07E-06			0		
66	Dy	155	4.53E-04	1.77E-05			1.31E-04	3.466	
67	Ho	156	5.21E-04	2.97E-05			4.79E-04	1.087	0.278
66	Dy	157	6.16E-04	1.38E-05			4.36E-05	14.135	
63	Eu	157	6.57E-06	9.83E-07			0		
68	Er	160	1.88E-03	1.12E-05			4.79E-04	3.924	
69	Tm	161	9.48E-04	8.14E-05			6.54E-04	1.45	
68	Er	161	9.64E-04	6.16E-06			1.31E-04	7.359	0.738
69	Tm	162	2.43E-03	9.60E-05			6.10E-04	3.984	2.619
69	Tm	163	8.80E-04	1.74E-05			4.79E-04	1.837	0.382
69	Tm	164	2.20E-03	1.35E-04			2.18E-04	10.092	
71	Lu	165	1.78E-04	2.49E-05			1.13E-03	0.158	0.257
69	Tm	165			6.94E-04	8.14E-06	2.61E-04	2.659	1.235
71	Lu	166	1.47E-03	5.32E-04			9.15E-04	1.607	1.996
70	Yb	166	6.40E-04	9.15E-05			3.93E-04	1.631	
69	Tm	166	3.35E-05	5.16E-07			4.35E-05	0.77	6.301
71	Lu	167			4.12E-04	6.38E-05	6.97E-04	0.591	0.342
69	Yb	167			1.78E-03	8.85E-05	4.36E-05	40.734	
73	Ta	169	2.33E-04	1.05E-05			1.18E-03	0.197	
71	Lu	169			2.00E-03	1.86E-05	8.28E-04	2.415	2.126
70	Yb	169	2.32E-03	2.45E-05			2.18E-04	10.642	
72	Hf	170	2.26E-03	2.74E-05			1.05E-03	2.152	0.461
71	Lu	170	2.11E-04	2.28E-06			4.79E-04	0.441	
72	Hf	171	2.38E-03	1.05E-04			6.97E-04	3.415	0.105
71	Lu	171	6.37E-04	7.58E-06			3.04E-04	2.095	0.12
68	Er	171	9.77E-06	1.05E-06			0		
73	Ta	172	1.32E-03	7.42E-05			1.57E-03	0.841	2.478
72	Hf	172	1.63E-03	5.42E-05			6.54E-04	2.492	
71	Lu	172	1.89E-04	6.33E-06			4.36E-05	4.335	
73	Ta	173	1.84E-03	8.29E-06			1.95E-03	0.944	0.473
72	Hf	173	1.75E-03	2.89E-05			3.92E-04	4.464	2.029
74	W	174	1.48E-04	1.59E-05			2.00E-03	0.074	0.17
73	Ta	174	1.34E-04	1.79E-06			1.22E-03	0.11	0.507
73	Ta	175	2.76E-03	1.51E-04			1.57E-03	1.758	1.132
73	Ta	176	2.97E-03	3.19E-05			1.18E-03	2.517	1.202
74	W	177	1.52E-03	6.30E-06			1.79E-03	0.849	0.562
75	Re	178	6.30E-04	2.37E-05			6.10E-04	1.033	0.819
74	W*	178	1.39E-04	1.19E-05			3.14E-03	0.044	0.037
73	Ta	178	9.11E-04	4.22E-06			8.28E-04	1.1	
71	Lu	178	8.81E-05	2.56E-05			4.36E-05	2.021	
75	Re	179	1.08E-03	4.64E-05			6.97E-04	1.549	1.46
72	Hf	179	1.74E-05	9.11E-07			8.71E-05	0.2	
75	Re	180	9.93E-04	7.29E-05			6.54E-04	1.518	0.733
75	Re	181	5.74E-04	9.96E-06			8.71E-04	0.659	
72	Hf	181	5.62E-05	1.76E-06			2.18E-04	0.258	
75	Re	182	4.28E-04	7.43E-06			2.61E-04	1.64	14.029

73	Ta	182	3.11E-04	1.16E-04	1.53E-03	0.204	
73	Ta	183	5.59E-04	4.58E-06	1.48E-03	0.378	
75	Re	184	1.28E-04	1.78E-06	2.61E-04	0.49	
73	Ta	184	2.12E-04	2.86E-06	3.04E-04	0.697	0.611
74	W	187	3.75E-03	1.92E-05			0.484

Table 3C Tungsten Spallation Yields for Position 6A

Z	Sym	A	Independent Yield n/cc/p	+/-	Cumulative Yield n/cc/p	+/-	Calculated (LAHET)	Ratio LAHET	Ratio CINDER'90
65	Tb	154	1.91E-04	7.09E-06			4.36E-05	4.388	8.37
65	Tb	155	7.68E-04	4.73E-05			8.77E-05	8.753	
68	Er	155	1.83E-05	8.24E-07			1.74E-04	0.105	
66	Dy	155			1.83E-05	8.24E-07			5.53
68	Er	161			1.58E-04	3.52E-06			0.30
69	Tm	162	2.28E-04	2.97E-05			1.74E-04	1.308	2.74
70	Yb	162	2.15E-04	2.88E-05			4.35E-05	4.941	
69	Tm	165			4.40E-04	4.21E-06			2.62
69	Tm	166			4.74E-04	7.32E-06	4.36E-05		
71	Lu	167					5.22E-04		
72	Hf	167	1.66E-04	1.31E-05			4.79E-04	0.347	0.53
71	Lu	169	6.91E-05	1.99E-06			4.36E-05	1.586	
72	Hf	169	5.98E-04	7.18E-06			2.61E-04	2.291	
73	Ta	169	2.88E-04	4.86E-05			2.18E-04	1.322	
71	Lu	170	1.78E-04	1.59E-06			1.74E-04	1.022	
72	Hf	170			7.77E-04	4.61E-06	4.36E-04		0.63
73	Ta	170	1.00E-03	6.12E-05			3.92E-04	2.554	
71	Lu	172	5.51E-05	1.43E-06			0		
72	Hf	172			1.22E-03	6.23E-05	2.61E-04		
73	Ta	172			7.86E-04	1.49E-05	3.49E-04		2.54
72	Hf	173			1.28E-03	8.61E-06	2.18E-04		
74	W	173	1.50E-03	5.85E-05			7.83E-04	1.915	
73	Ta	175			1.25E-03	7.05E-06	4.79E-04		0.54
73	Ta	176			1.21E-03	1.32E-05	3.92E-04		
74	W	177	1.33E-03	8.00E-06			9.58E-04	1.388	0.75
75	Re	179	4.39E-04	1.33E-05			2.61E-04	1.679	
72	Hf	180	2.46E-03	1.93E-04			1.31E-04	18.851	526.35
75	Re	180	2.38E-04	1.33E-05			3.92E-04	0.608	
76	Os	180	4.59E-05	5.42E-06			0		
72	Hf	181	1.70E-05	4.58E-07			0		
75	Re	181	2.13E-04	2.08E-06			5.66E-04	0.376	
73	Ta	182	6.71E-04	1.00E-04			2.18E-04	3.081	
75	Re	182	2.47E-04	4.15E-06			8.71E-05	2.836	
73	Ta	183	2.05E-04	1.17E-06			3.49E-04	0.589	
76	Os	183	3.97E-05	4.05E-06			0		
73	Ta	184	8.59E-05	1.07E-06			1.31E-04	0.657	0.65
75	Re	184	5.77E-05	6.42E-07			1.74E-04	0.331	
73	Ta	185			4.53E-04	9.23E-05	2.61E-04		1.83
74	W	187							0.34

Table 3D Tungsten Spallation Yields for Position 8A

Z	Sym	A	Independent Yield n/cc/p	+/-	Cumulative Yield n/cc/p	+/-	Calculated (LAHET)	Ratio LAHET	Ratio CINDER'90
63	Eu	146	6.87E-07	8.12E-08					
65	Tb	156	1.76E-05	1.84E-07					
71	Lu	169	1.37E-05	1.79E-06					
72	Hf	170	2.29E-05	5.31E-06			4.36E-05	0.525	
71	Lu	171	2.56E-05	3.50E-07					
71	Lu	172	3.53E-06	3.10E-07				#DIV/0!	
73	Ta	172					1.31E-04	0.000	5.56
73	Ta	174	7.41E-05	2.85E-06			1.31E-04	0.566	
73	Ta	175	9.07E-05	5.63E-06			1.74E-04	0.521	0.084
74	W	176	1.22E-04	2.34E-06			5.23E-04	0.233	
74	W	177	4.14E-04	4.07E-06			3.92E-04	1.056	0.614
73	Ta	178	2.28E-05	5.04E-07			4.36E-05	0.523	
75	Re	178	2.21E-04	4.44E-06			2.18E-04	1.014	0.93
75	Re	179	3.94E-04	6.48E-06			8.71E-05	4.524	
75	Re	181	4.52E-04	3.36E-06			4.35E-05	10.391	12.830
75	Re	182	1.70E-03	6.86E-05			8.71E-05	19.518	0.788
73	Ta	183	3.35E-05	2.40E-07			4.36E-05	0.768	
73	Ta	184	1.37E-05	9.73E-07					
75	Re	184	1.00E-04	8.61E-07			8.71E-05	1.148	
74	W	187	1.08E-03	7.31E-06					6.23E-00

Table 3E Tungsten Spallation Yields for Position 4B

Z	Sym	A	Independent Yield n/cc/p	"+/-"	Cumulative Yield n/cc/p	"+/-"	Calculated (LAHET)	Ratio LAHETt
66	Dy	155	4.94E-06	6.69E-07			0.00E+01	
68	Er	161	1.70E-05	2.16E-06			0.00E+01	
69	Tm	165			2.70E-05	7.33E-07	0.00E+01	
71	Lu	169			5.39E-05	1.16E-06	6.82E-05	0.791
72	Hf	170			6.39E-05	8.16E-07	1.02E-04	0.627
71	Lu	170	4.79E-06	1.41E-07			0.00E+01	0.745
72	Hf	171			3.99E-06	7.70E-08	1.02E-04	0.039
71	Lu	171			9.22E-05	4.31E-03	3.41E-05	2.702
73	Ta	173	9.31E-05	1.78E-05			1.03E-04	0.909
72	Hf	173	5.52E-05	9.58E-07			0.00E+01	
73	Ta	175			1.70E-04	2.78E-06	2.39E-04	0.712
73	Ta	176			2.97E-04	2.74E-06	1.02E-04	2.912
75	Re	181			3.24E-05	4.05E-07	3.41E-05	0.950
75	Re	182	1.46E-05	4.90E-07			0.00E+01	
73	Ta	183	7.37E-05	4.56E-07			3.41E-05	2.160
73	Ta	184	3.00E-05	3.62E-07			0.00E+01	
74	W	187	2.94E-03	2.04E-06			0.00E+01	

Table 3F Tungsten Spallation Yields for Position 8B

Z	Sym	A	Independent Yield n/cc/p	"+/-"	Cumulative Yield n/cc/p	"+/-"	Calculated (LAHET)	Ratio LAHET
71	Lu	166	1.49E-06	2.23E-07				
72	Hf	166	7.71E-07	1.54E-07				
70	Yb	169	4.78E-06	7.06E-08				
71	Lu	169	6.52E-06	9.78E-07				
72	Hf	169			8.75E-06	3.77E-07	6.82E-05	0.128
71	Lu	170			1.45E-05	4.85E-07		
71	Lu	171			1.59E-05	1.08E-07	3.41E-05	0.466
71	Lu	172	1.67E-06	4.39E-08				
72	Hf	172	1.32E-05	3.03E-06			3.41E-05	0.387
73	Ta	172	2.41E-05	3.79E-06				
71	Lu	173	2.63E-05	2.09E-06				
72	Hf	173			2.82E-05	5.50E-07		
73	Ta	174	9.97E-06	1.99E-07			6.82E-05	0.146
74	W	174	2.31E-05	4.63E-06			6.82E-05	0.339
73	Ta	175			3.35E-05	1.73E-06	1.02E-04	0.328
73	Ta	176			5.39E-05	1.58E-06	1.02E-04	0.528
75	Re	176	5.06E-06	4.74E-07				
74	W	177	8.49E-05	1.73E-06			2.04E-04	0.416
73	Ta	178			1.58E-05	2.12E-07	3.41E-05	0.463
75	Re	178	6.43E-05	1.05E-06			6.82E-05	0.943
72	Hf	179	3.51E-07	4.16E-08				
74	W	179	3.26E-05	1.53E-06			1.70E-04	0.192
75	Re	179	1.14E-04	6.58E-07			1.36E-04	0.838
75	Re	180	1.01E-04	2.58E-06			6.82E-05	1.481
72	Hf	181	1.29E-06	7.30E-08				
75	Re	181	6.84E-05	1.01E-06			1.02E-04	0.671
73	Ta	182			1.59E-05	4.53E-07	3.41E-05	0.466
75	Re	182	5.23E-05	1.17E-05			3.41E-05	1.534
73	Ta	183			1.79E-05	1.35E-07	6.82E-05	0.262
75	Re	183	6.14E-05	9.41E-07				
73	Ta	184	7.12E-06	3.84E-07				
75	Re	184	8.41E-04	2.06E-07			3.41E-05	24.663
74	W	187	8.86E-04	2.61E-06				

The data can be summarized in several ways. Figure 15 shows mass yields, the yields summed over all Z for a given mass, compared to LAHET calculations. The dashed histogram indicates the calculated sum over all nuclei, the solid histogram is the calculated sum over only those nuclei that were observed. The solid line should be compared to the data. The calculations predict a more rapid decrease with mass for foils deeper into the W assembly, corresponding to increasing energy loss of the proton beam. This is consistent with the trend of the data. Measurements one mass unit above the stable W isotopes (^{182}W, ^{183}W, ^{184}W, and ^{186}W. ^{180}W is also stable, but is only 0.13% abundant) are underpredicted by the LAHET calculations. The production of these isotopes is dominated by neutron capture on the stable isotopes, and therefore is not a spallation process, but is calculated by CINDER'90[15] In Fig 15A, for position 2A, we note a deviation from the LAHET calculations for low masses which is probably due to fission production of these nuclei.

Figure 16 show the charge dispersion, or yield as a function of Z, for a given mass. The histograms are the LAHET calculations, and the dashed curves are the empirical paramaterization of Summerer[16], normalized to the maximum of the LAHET distribution. In general, the calculations reproduce the trend of the empirical paramaterization, which both are in reasonable agreement with the overall trends of the data, although there are disagreements in detail.. In both masses 178 and 180, the Summerer curve is displaced to higher Z from the LAHET calculation and the data. This may be due to an inadequate paramterization of the "memory effect" for products close to the target mass. It was noted by Summerer the memory effect parameters in his work were based on only two data sets.

Next we consider in detail the comparison of calculations and measurements for individual nuclei. Figure 17 shows the LAHET yield calculations as a function of Z and A for each of the foil positions we are reporting. Figure 18 shows the measured yields, and Figure 19 shows the ratios of measured yield to LAHET. Figure 20 shows the ratios of the measured yields to the CINDER'90 calculations. Because of the complex gamma spectra, there are fewer analyzable comparisons to the CINDER'90 calculations. These comparisons are summarized in the histograms of figures 21 and 22.

5b. Isotopes assumed in BDBE Calculation

This section studies the production of radioisotopes considered to be important in the Beyond Design Basis Event (BDBE) environmental source term for the tungsten target. Table 4A is an overview and directs the reader to Tables 4B and 4C which contain more detailed information on BDBE isotopes measured in this program. The isotopes are listed in order of importance in Table 4A, the column labeled *Comments* contains either a comment number, which is described below the table, or a minimum detectable limit of the isotope in

this experiment. The limit was estimated for position 2A during a 1 hour irradiation. The *CINDER'90* column, for isotopes which were not detected, contains the quantity calculated to be produced in the target at position 2A at end of bombardment of a 1 hour irradiation. The zeros in this column are due to the statistics of the Monte Carlo calculation, and do not necessarily indicate zero production.

TABLE 4A Summary of isotopes in BDBE calculation

Isotope	Comment	CINDER'90 calculation
H-3	1	1.25 E-07 Nuc/cc/p
W-185	3	2.21 E-03 Nuc/cc/p
W-187	2	4
W-181	3	1.83 E-03 Nuc/cc/p
Xe-127	< 4.93 E-05 Nuc/cc/p	0.00 E-00 Nuc/cc/p
W-178	2, 3	4
Xe-125	< 7.23 E-06 Nuc/cc/p	8.24 E-06 Nuc/cc/p
Ar-37	1	0.00 E-00 Nuc/cc/p
Kr-79	< 4.61 E-05 Nuc/cc/p	4.49 E-06 Nuc/cc/p
Xe-122	< 3.26 E-05 Nuc/cc/p	8.93 E-06 Nuc/cc/p
W-177	2	4
W-176	2	4
Cs-131	1	0.00 E-00 Nuc/cc/p
Xe-129m	< 7.67 E-05 Nuc/cc/p	0.00 E-00 Nuc/cc/p
Xe-123	2	4
I-122	< 2.79 E-05 Nuc/cc/p	1.80 E-06 Nuc/cc/p
I-131	< 1.67 E-05 Nuc/cc/p	0.00 E-00 Nuc/cc/p
I-133	< 3.09 E-06 Nuc/cc/p	0.00 E-00 Nuc/cc/p
I-135	< 4.05 E-05 Nuc/cc/p	0.00 E-00 Nuc/cc/p

(1) Can not measure, this can be due to unfavorable half-life, decay or gamma-ray energy that makes detection impossible.
(2) Measured for at least one foil position, see Table 4B for complete details.
(3) Can not measure for same reasons as (1); however, the parent nuclide is observed and over time will decay to the BDBE isotope. Information regarding the parent nuclide is given in Table 4C.

Table 4B lists information for the five BDBE isotopes that were measured directly in this experiment. The ratio of the measurement to both LAHET and CINDER'90 calculations is given in the table. The isotope ^{187}W is produced by neutron capture, and is not found in the Lahet spallation calculation. ^{123}Xe was calculated to have a negligible spallation yield. The measured production of ^{187}W is only about half of the CINDER'90 calculation. The results are less conclusive for ^{177}W, but the measured yield is about 0.5 to 0.8 times that predicted by CINDER'90.

TABLE 4B Comparison of measured yields of observed BDBE isotopes to LAHET and CINDER'90 calculations

Z	Sym	A	Position	n/cc/p	"+/-"	Ratio to LAHET	"+/-"	Ratio to CINDER'90	"+/-"
74	W	187	2A	5.63E-03	4.22E-05			0.483	0.019
			4A	3.75E-03	1.92E-05			0.484	0.071
			6A	2.21E-03	1.05E-05			0.588	0.025
			8A	1.08E-03	7.31E-06			0.596	0.020
			4B	2.91E-03	1.95E-06				
			8B	8.86E-04	2.61E-06				
74	W	177	2A	4.09E-03	7.67E-05	1.121	0.021	0.849	0.044
			6A	2.23E-04	2.49E-06	0.233	0.003	0.816	0.021
			8A	4.14E-04	4.07E-06	1.054	0.010	0.506	0.025
			8B	8.49E-05	1.73E-06	0.416	0.008		
74	W	176	2A	5.25E-03	1.31E-03	1.218	0.304		
54	Xe	123	2A	4.68E-03	1.16E-04				

Evidence for the production of ^{178}W was obtained from estimating the magnitude of the parent correction in the decay of the 2.4 hour half-life state of ^{178}Ta. The literature reports the branching ratio for this transition as zero {NP A93 385(67)}, and we have therefore found evidence of a non-zero branching ratio. However, the value of the branching ratio could not be determined and therefore we cannot report a measured yield.

Table 4cCsummarizes information relating to the production of parent nuclides of the BDBE isotopes ^{181}W and ^{178}W. The BDBE isotopes were not observed, but their parents will decay to them over time . The parent information gives a minimum quantity of the BDBE isotope

that will be present in the target, as well as an estimate of the goodness of the calculations in this mass region. This table is otherwise similar to Table 4B. Table 4C also gives an estimate for ^{185}W obtained from the parent buildup observed in the decay of its daughter ^{185}Ta.

Table 4C Estimates of production of unobserved BDBE isotopes from their parent or daughter decays.

Z	Sym	A	Position	n/cc/p	"+/-"	LAHET	"+/-"	CINDER'90	"+/-"
73	Ta	185	2A	2.44E-03	6.83E-04	1.394	0.390	1.126	0.024
75	Re	181	2A	4.23E-03	5.67E-05	2.611	0.035	0.092	0.023
			4A	5.74E-04	9.66E-06	0.659	0.011		
			6A	2.09E-04	2.08E-06	0.368	0.004	1.893	0.215
			8A	4.52E-04	3.36E-06	10.371	0.077	12.499	2.855
			4B	3.24E-05	4.05E-07	0.950	0.012		
			8B	6.84E-05	1.01E-06	0.671	0.010		
75	Re	178	4A	6.30E-04	2.37E-05	1.033	0.039	0.819	0.061
			6A	1.47E-04	2.65E-05	0.675	0.122	2.290	0.756
			8A	2.21E-04	4.44E-06	1.014	0.020	1.027	0.230
			8B	6.43E-05	1.05E-06	1.886	0.031		

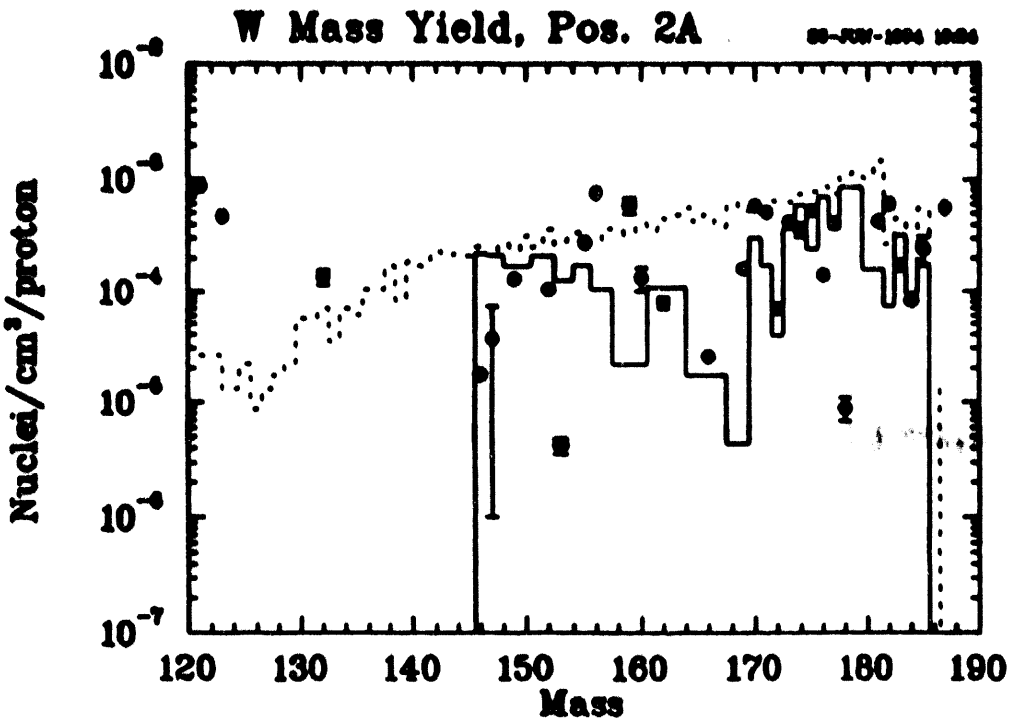

Fig. 15a. Observed mass yield for on-axis position 2A. The dashed histogram indicates the total masss yield calculated by LAHET. The solid histogram is the calculation summed over only the observed nuclei. The solid curve should bbe compared to thhe data.

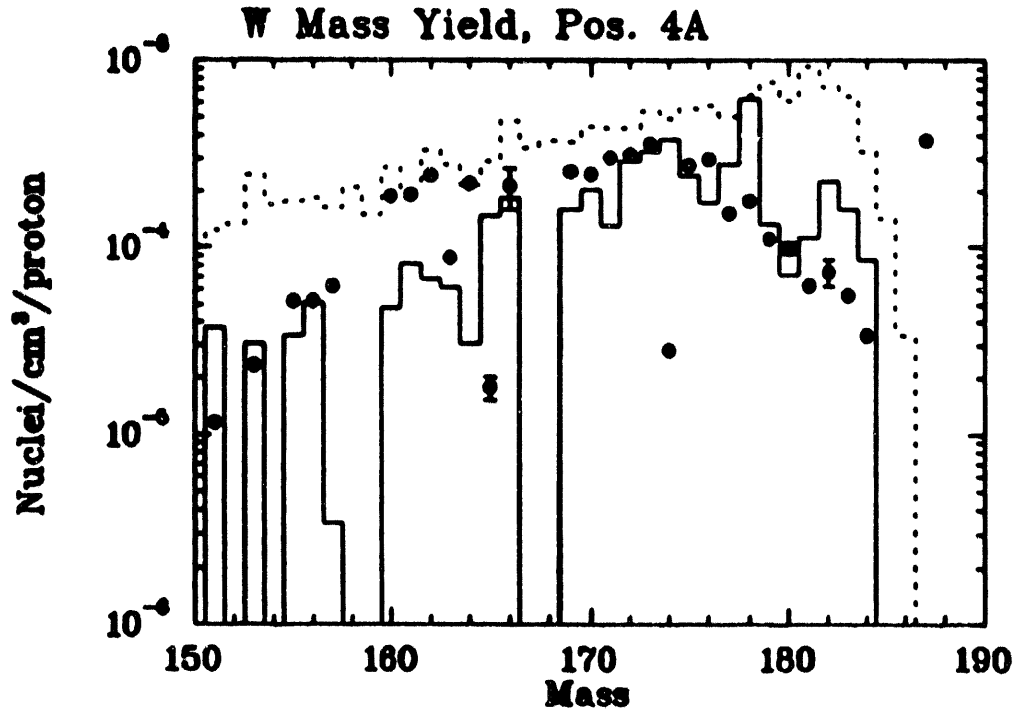

Fig. 15b. Mass yield for position 4A. Histograms same as in Fig. 15a.

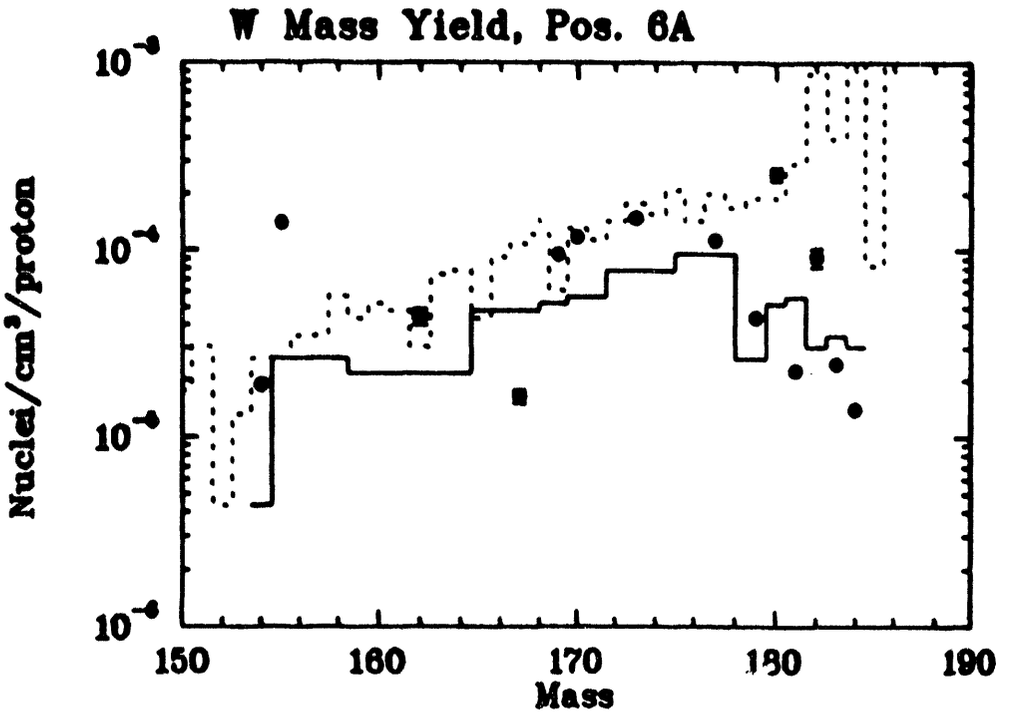

Fig. 15C. Mass yield for position 6A. Histograms same as in Fig. 15A.

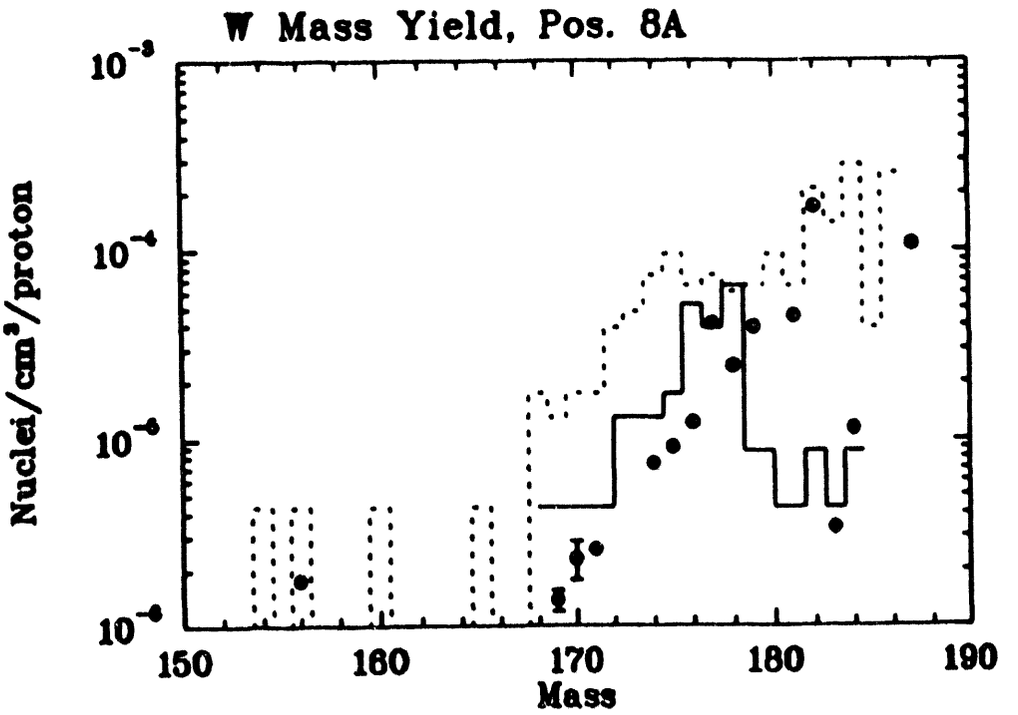

Fig. 15D. Mass yield for position 8A. Histograms same as in Fig. 15A.

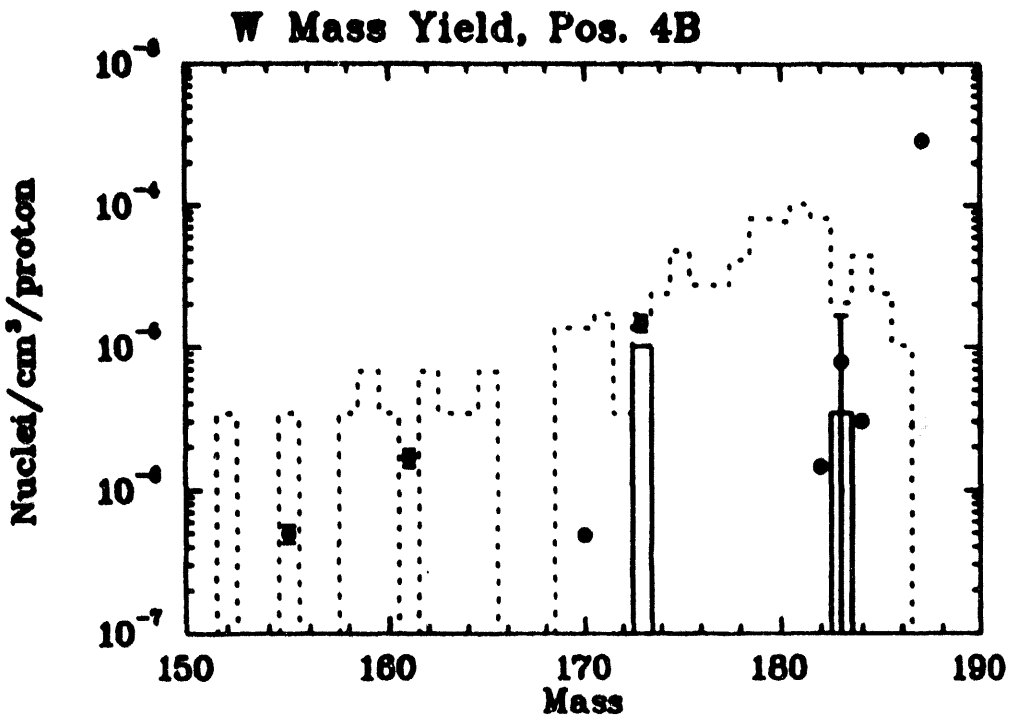

Fig. 15E. Mass yield for radial position 4B. Histograms same as in Fig. 15A.

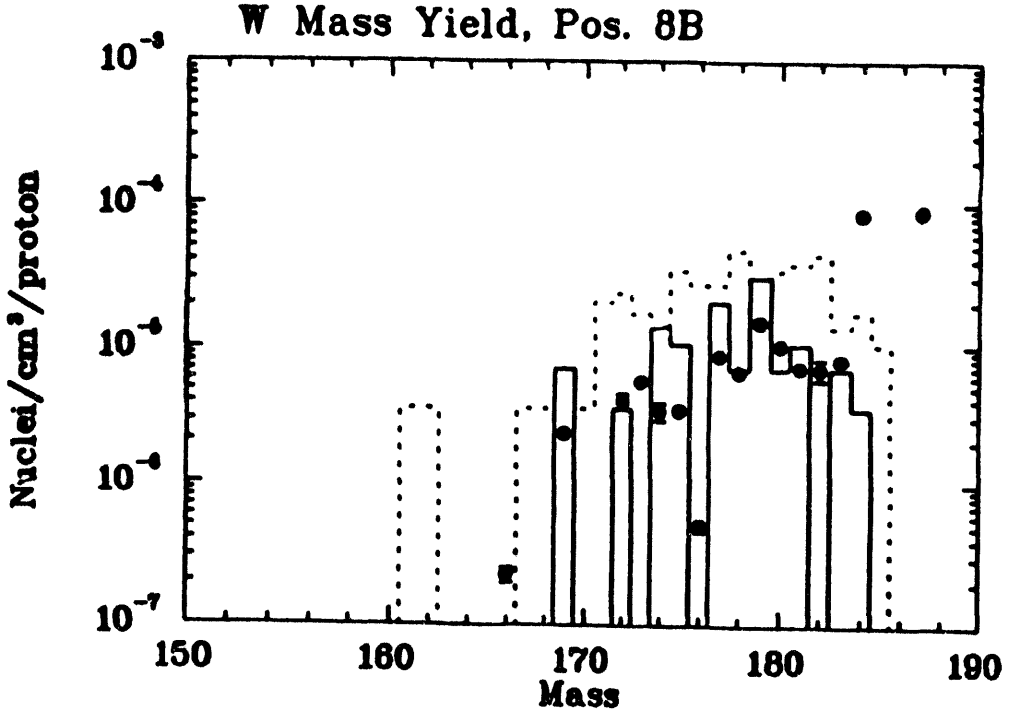

Fig. 15F. Mass yield for radial position 8B. Histograms same as in fig. 15A.

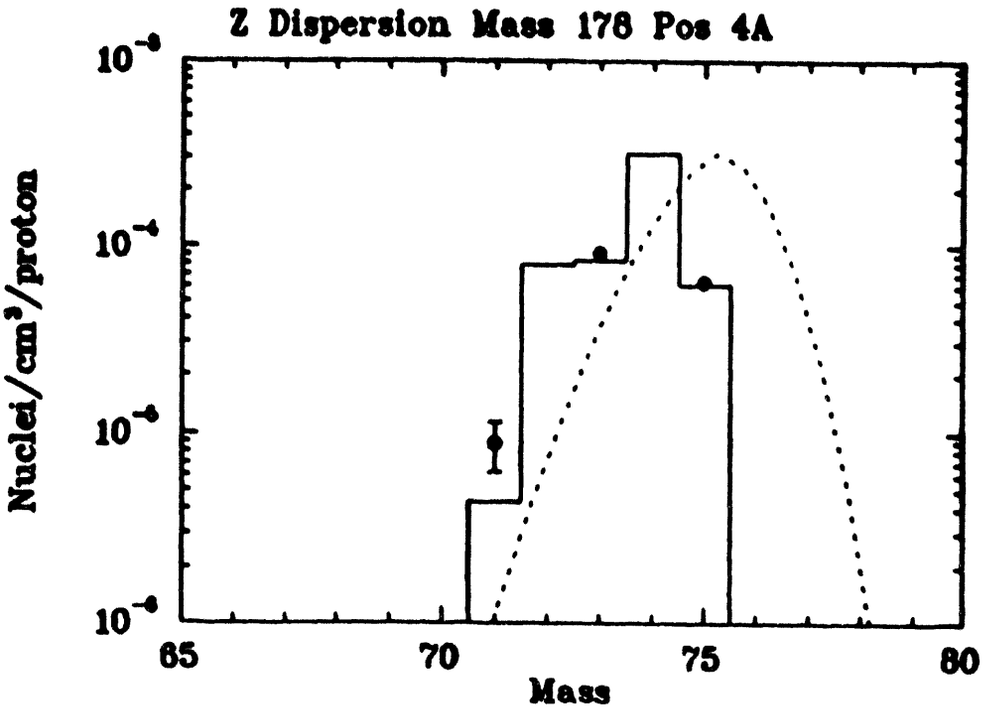

Figure 16A. Charge dispersion curve for mass 178. The histogram shows the LAHET calculated yields, the dashed line shows the Z dependence calculated using the Summerer systematics normalized to LAHET.

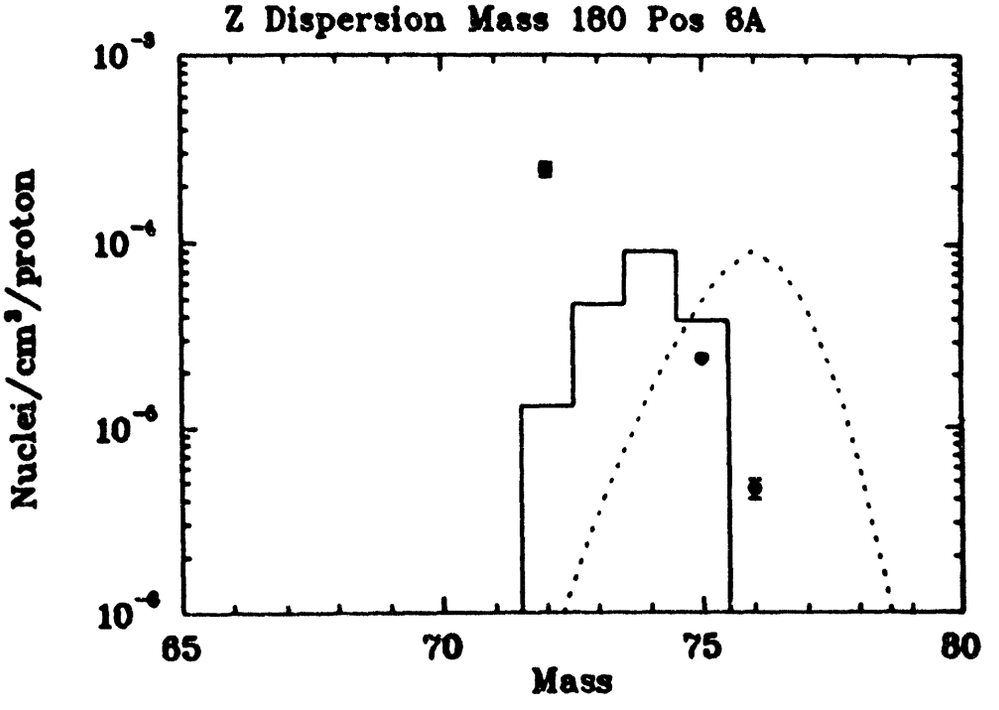

Figure 16B. Charge dispersion curve for mass 180. Curves as in 16A.

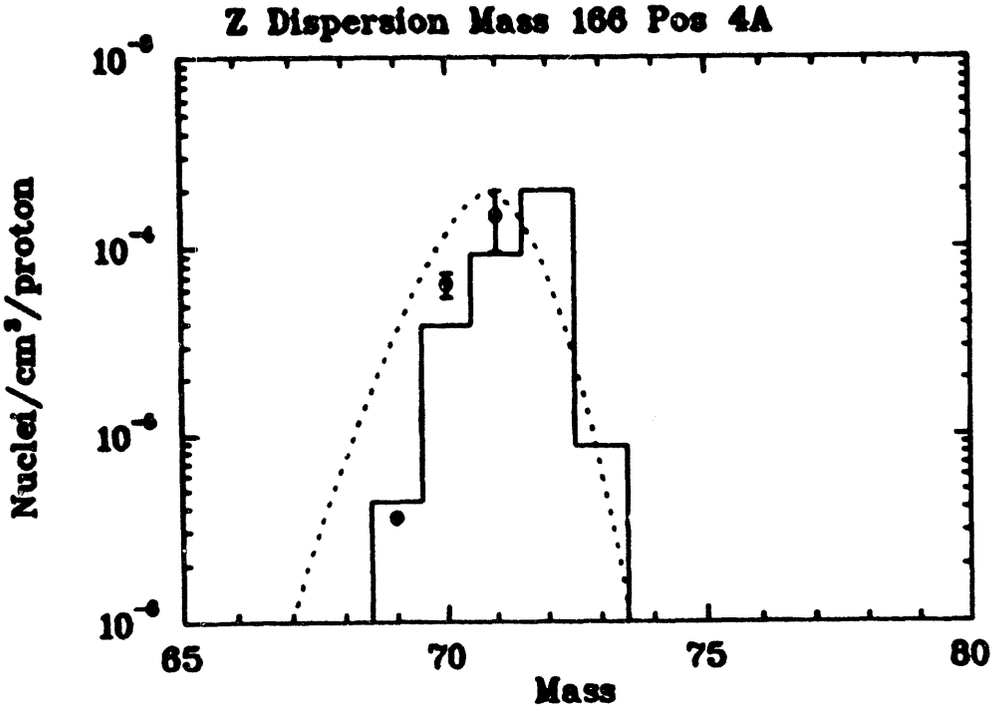

Figure 16C. Charge dispersion curve for mass 166. Curves as in 16A.

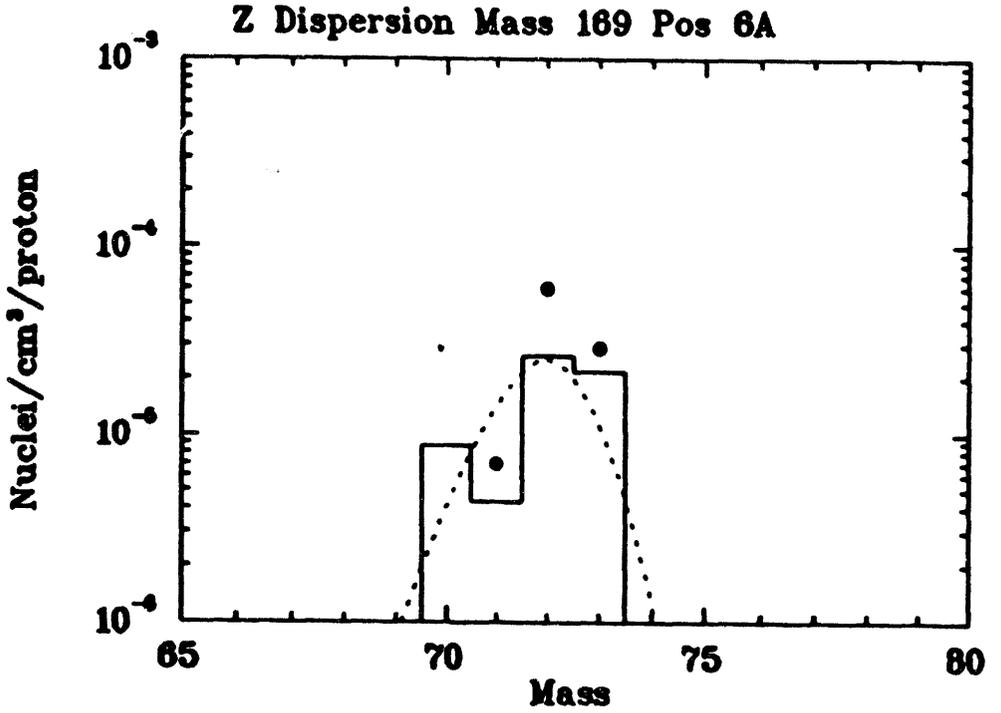

Figure 16D. Charge dispersion curve for mass 169. Curves as in 16A.

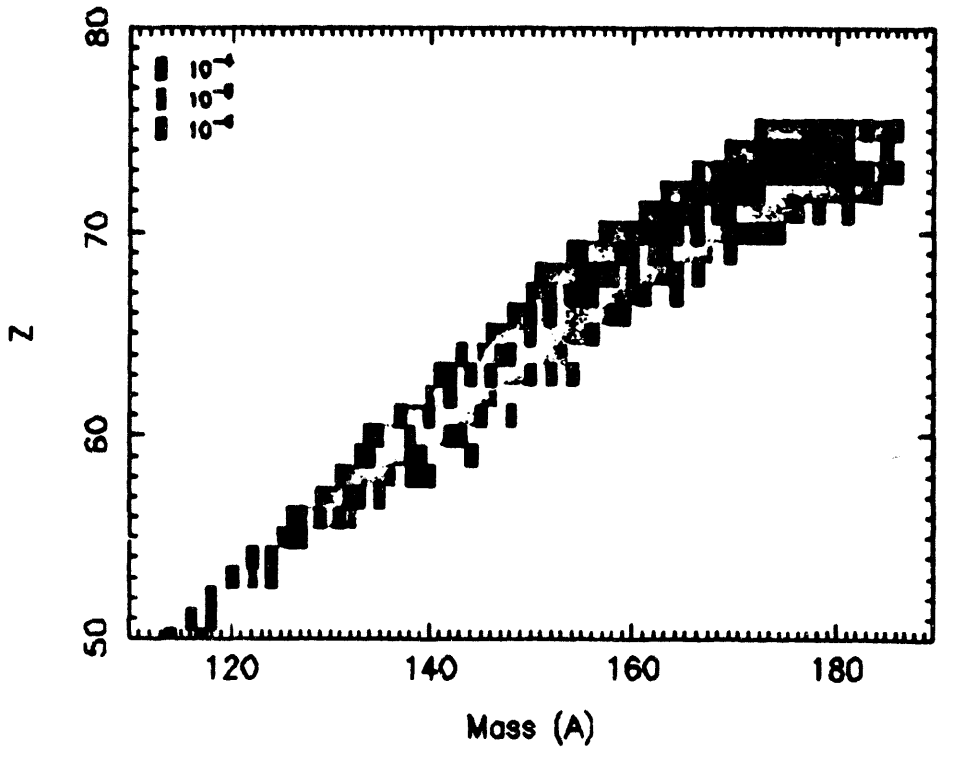

Fig 17A. Calculated LAHET yields for position 2A.

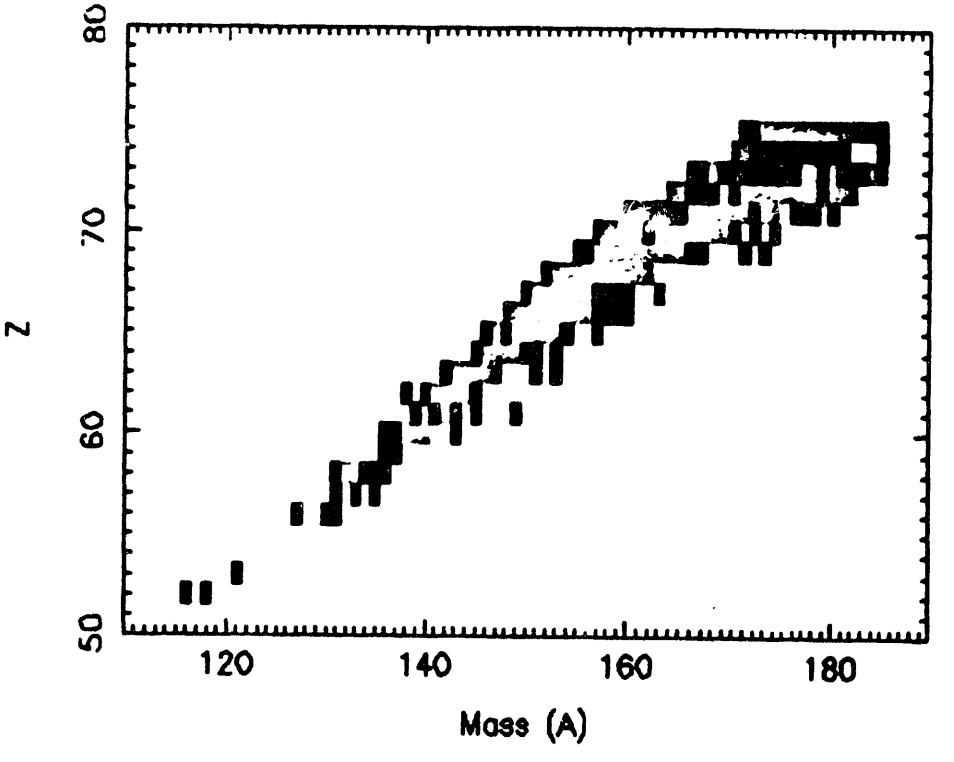

Fig 17B. Calculated LAHET yields for position 4A. Same scale as fig. 17A.

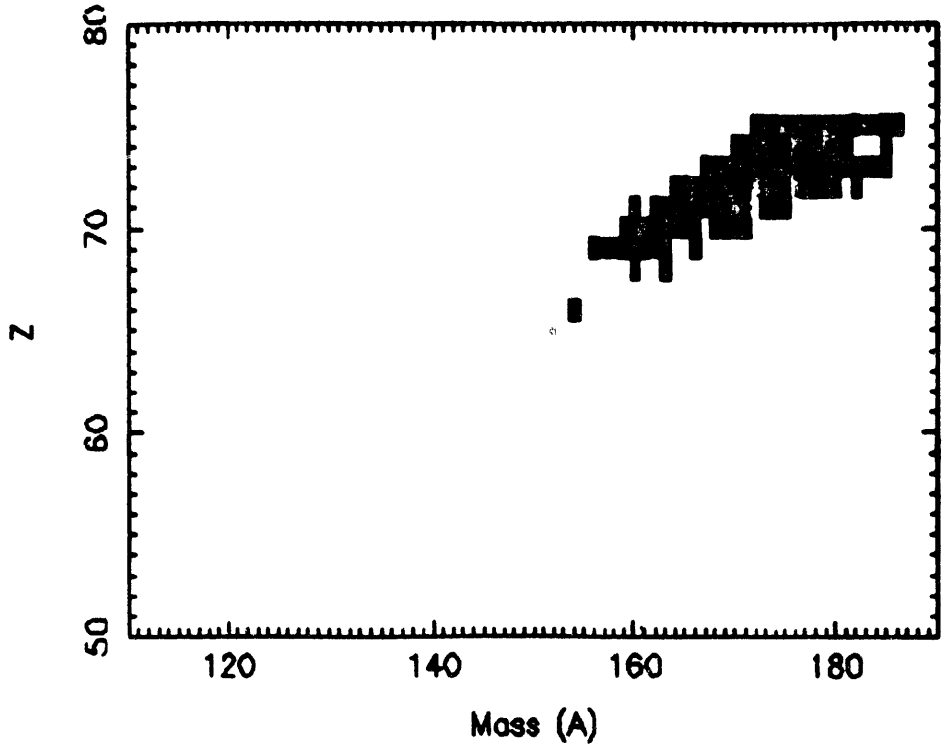

Fig 17C. Calculated LAHET yields for position 6A. Same scale as fig. 17A.

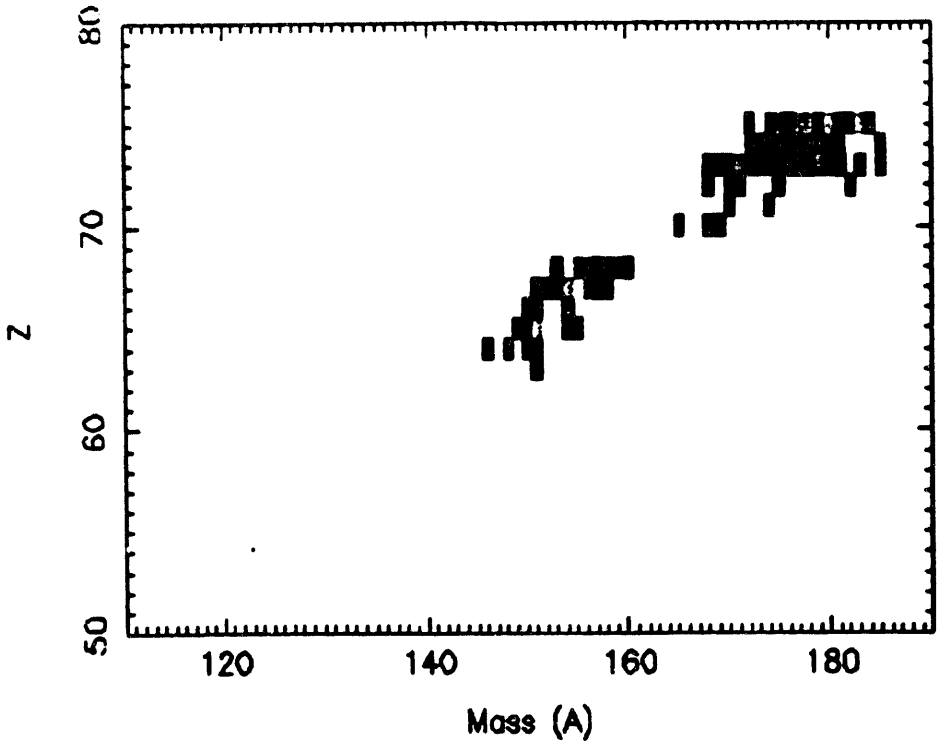

Fig 17D. Calculated LAHET yields for position 8A. Same scale as fig. 17A.

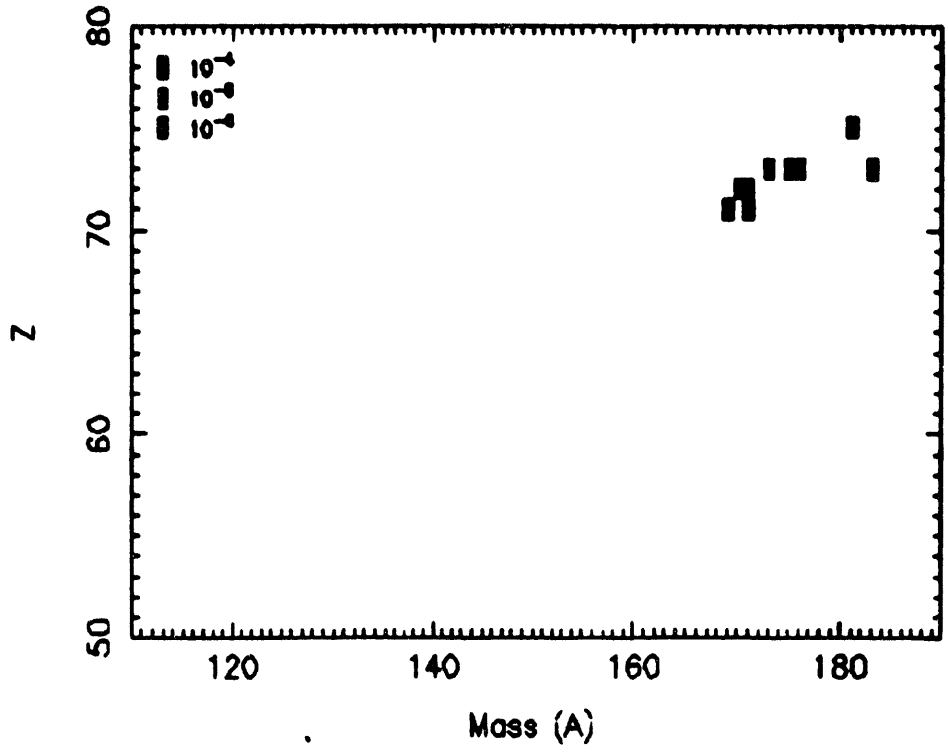

Fig 17EE. Calculated LAHET yields for position 4B. Same scale as fig. 17A.

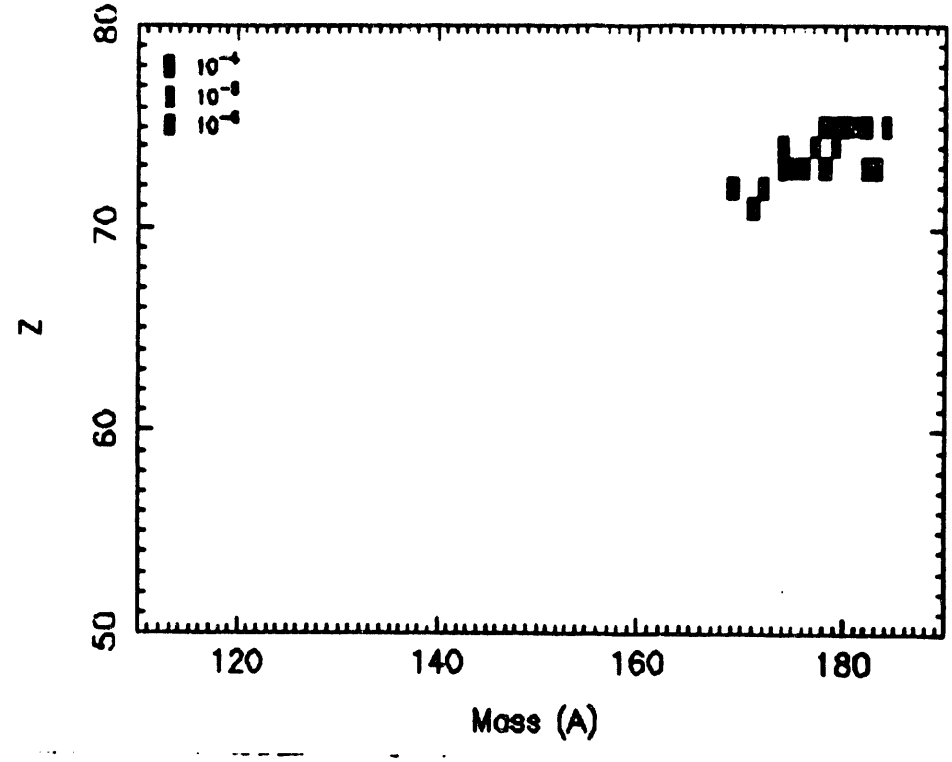

Fig 17F. Calculated LAHET yields for position 8B. Same scale as fig. 17A.

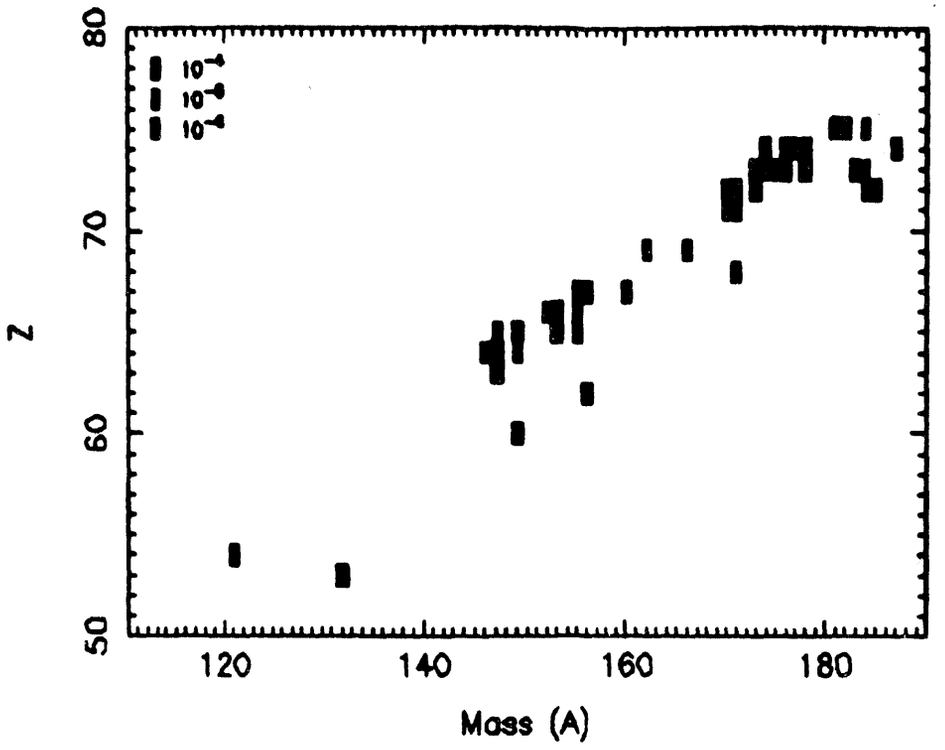

Fig. 18A Measured yield for position 2A

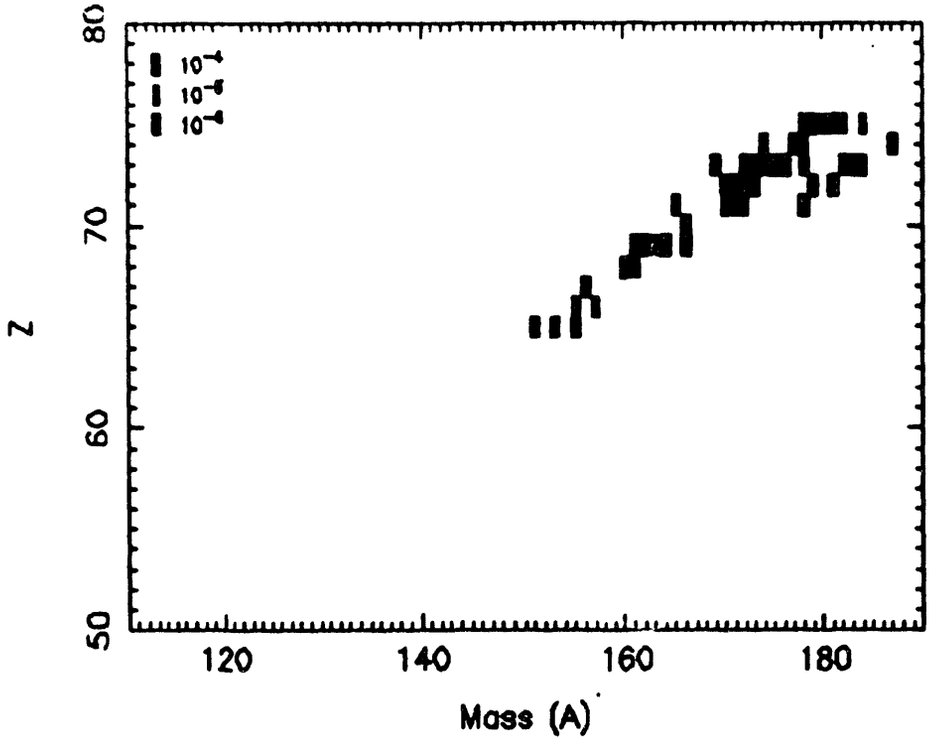

Fig 18B. Measured yield for position 4A. Same scale as Fig 18A.

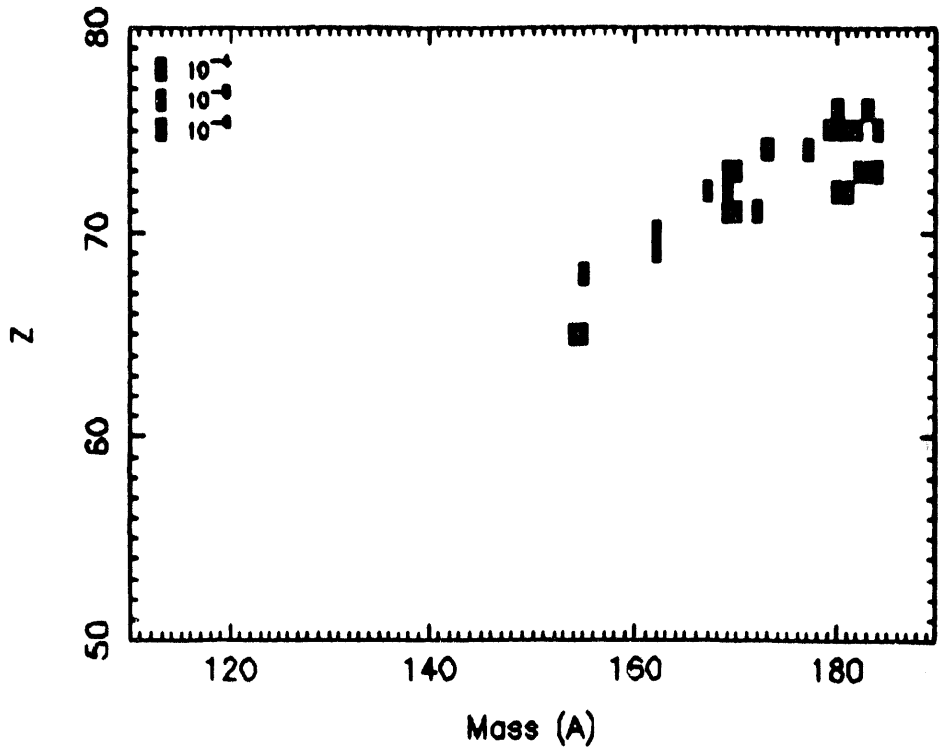

Fig 18C. Measured yield for position 6A. Same scale as Fig 18A

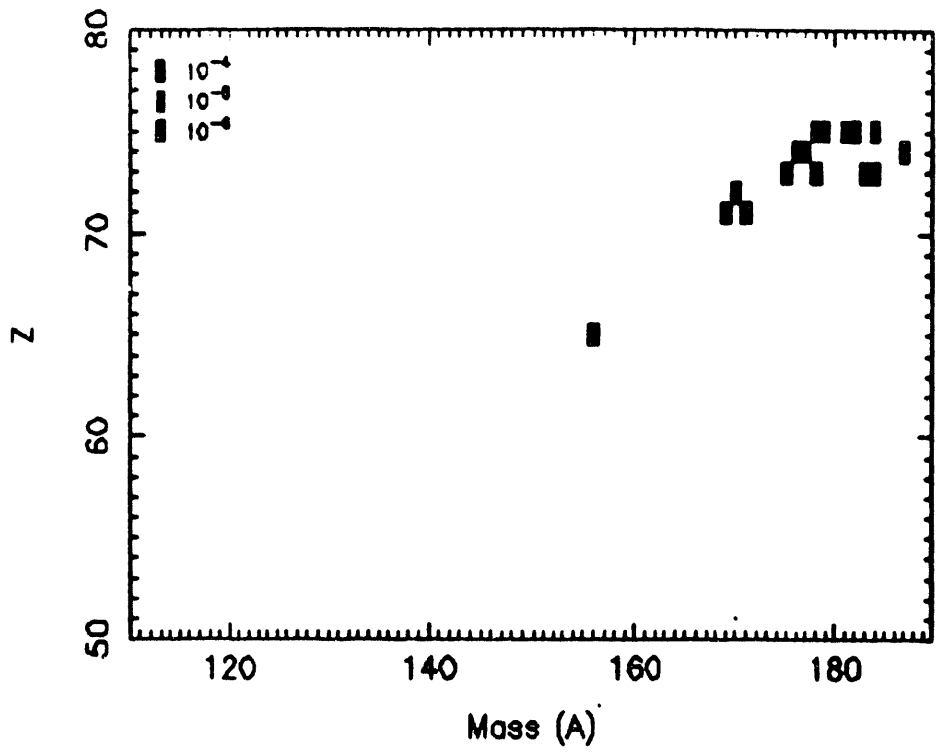

Fig 18D. Measured yield for position 8A. Same scale as Fig 18A.

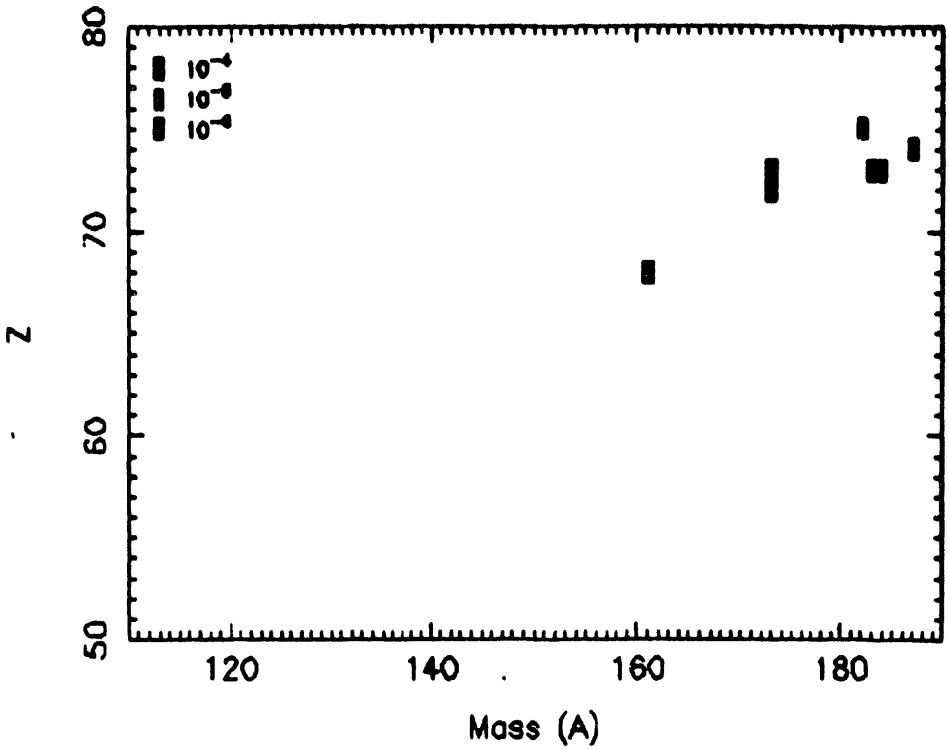

Fig 18E. Measured yield for position 4B. Same scale as Fig 18A

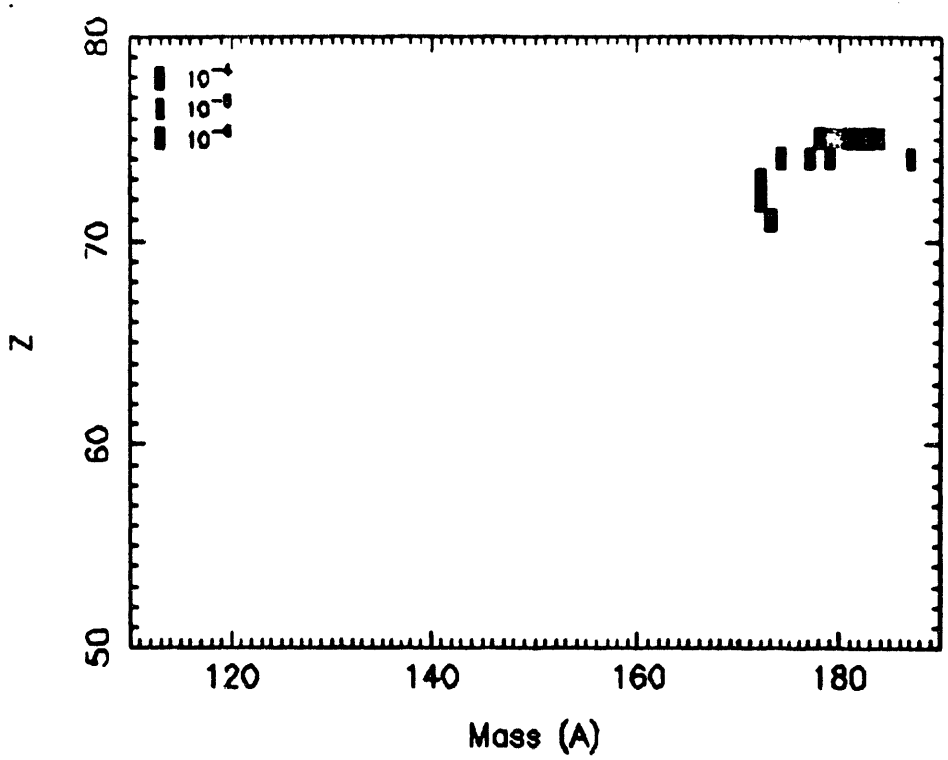

Fig 18F Measured yield for position 8B. Same scale as fig 18A

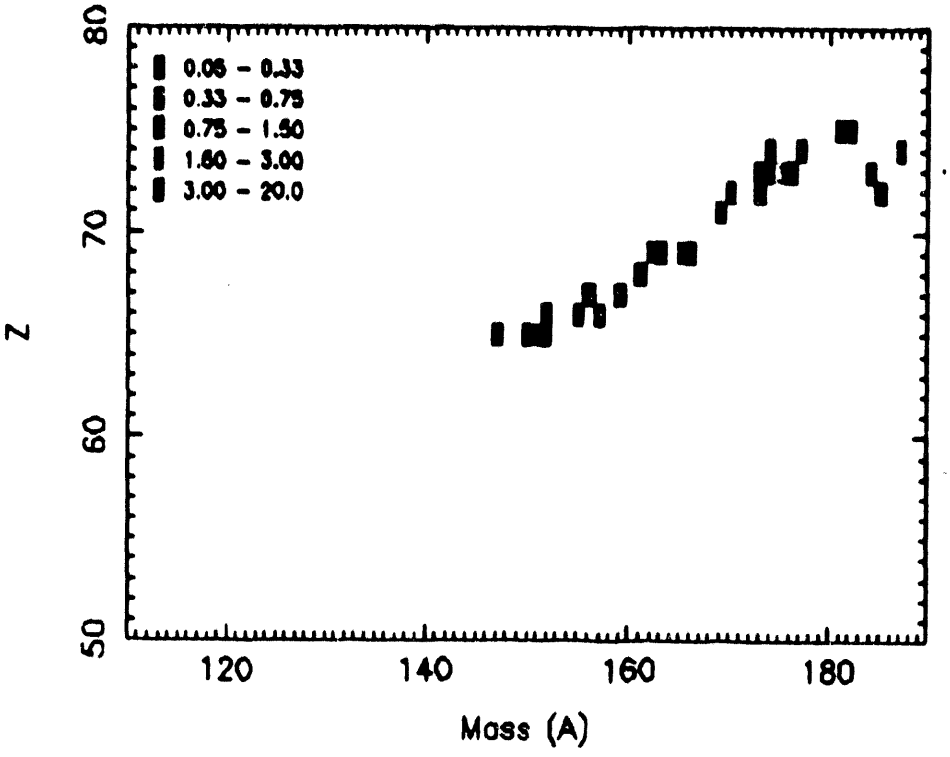

Fig. 19A. Ratio of measured yield to LAHET calculation for position 2A

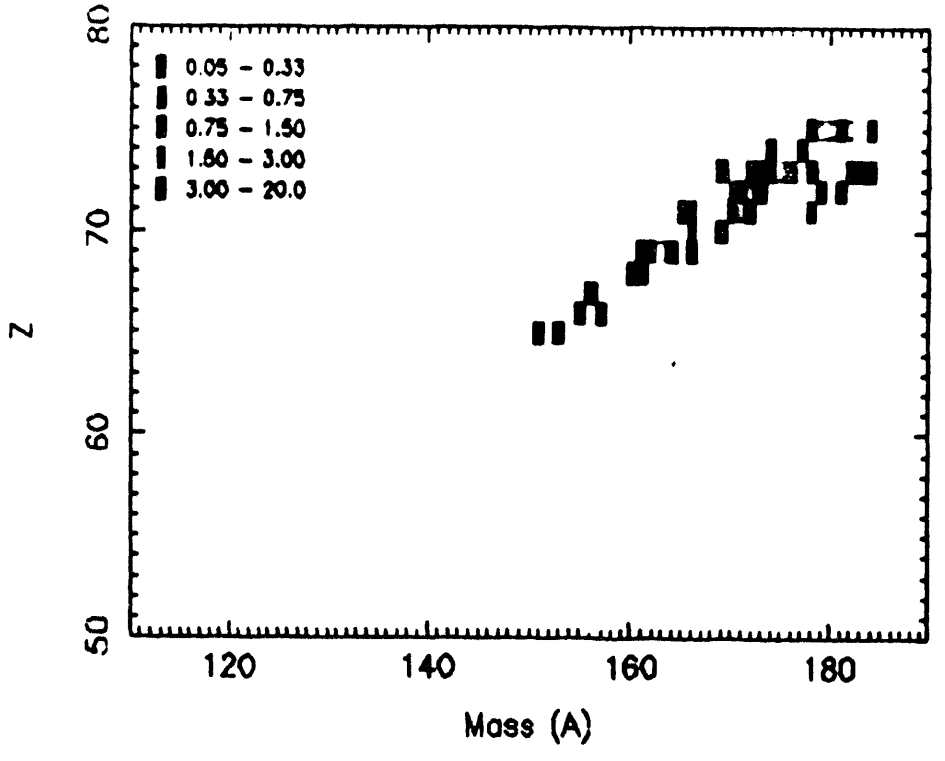

Fig. 19B. Ratio of measured yield to LAHET calculation for position 4A

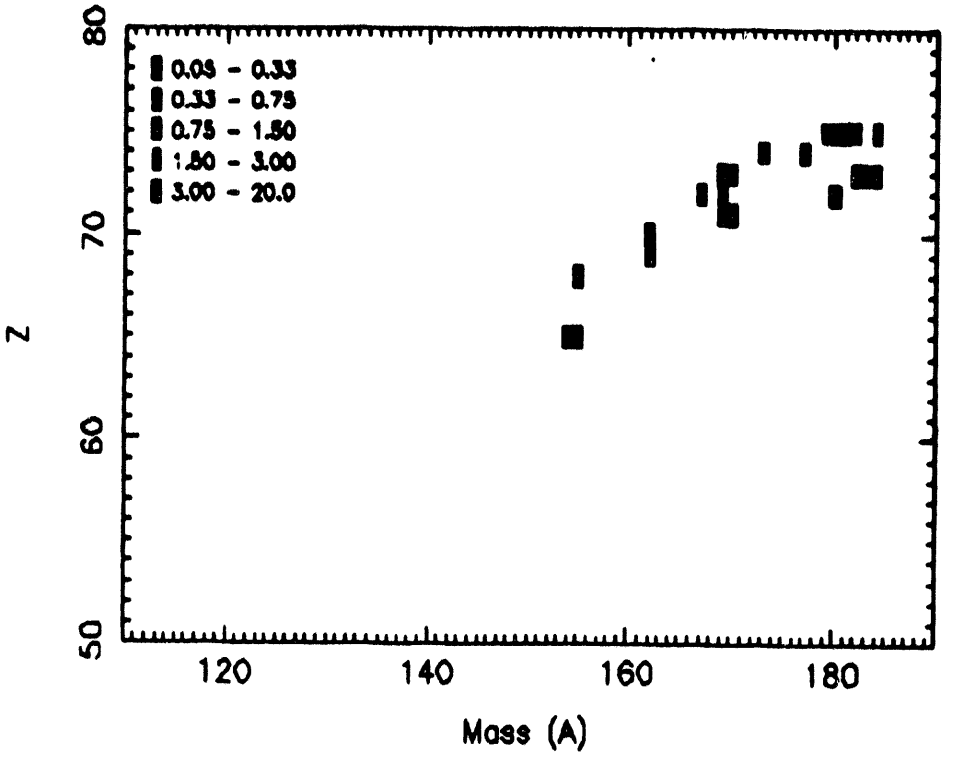

Fig. 19C. Ratio of measured yield to LAHET calculation for position 6A

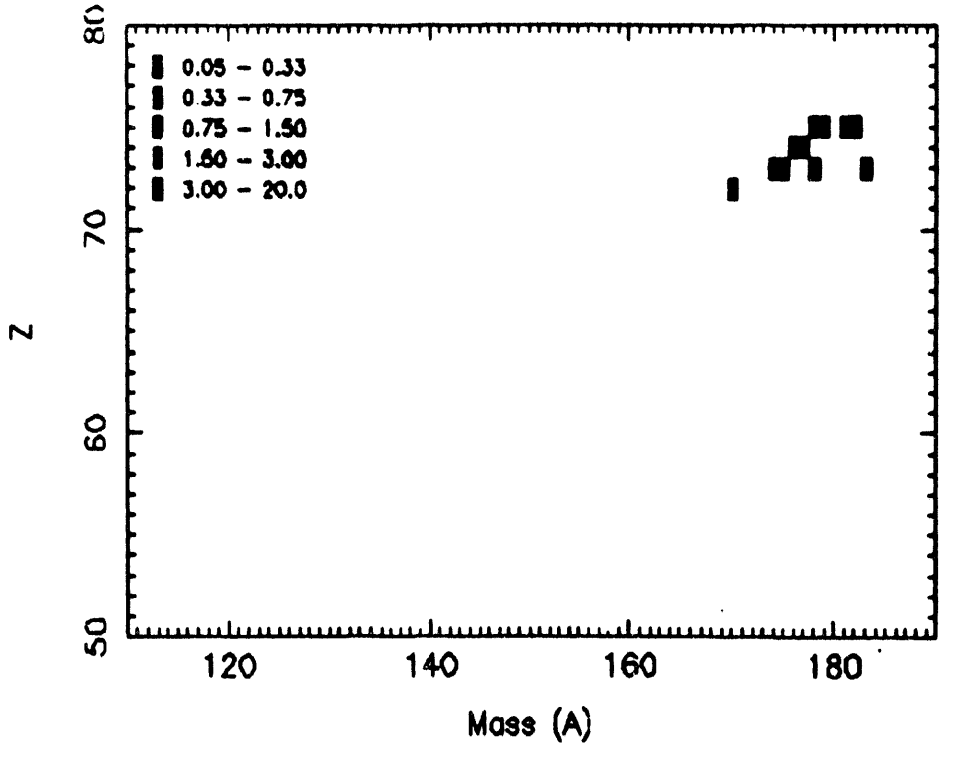

Fig. 19D. Ratio of measured yield to LAHET calculation for position 8A

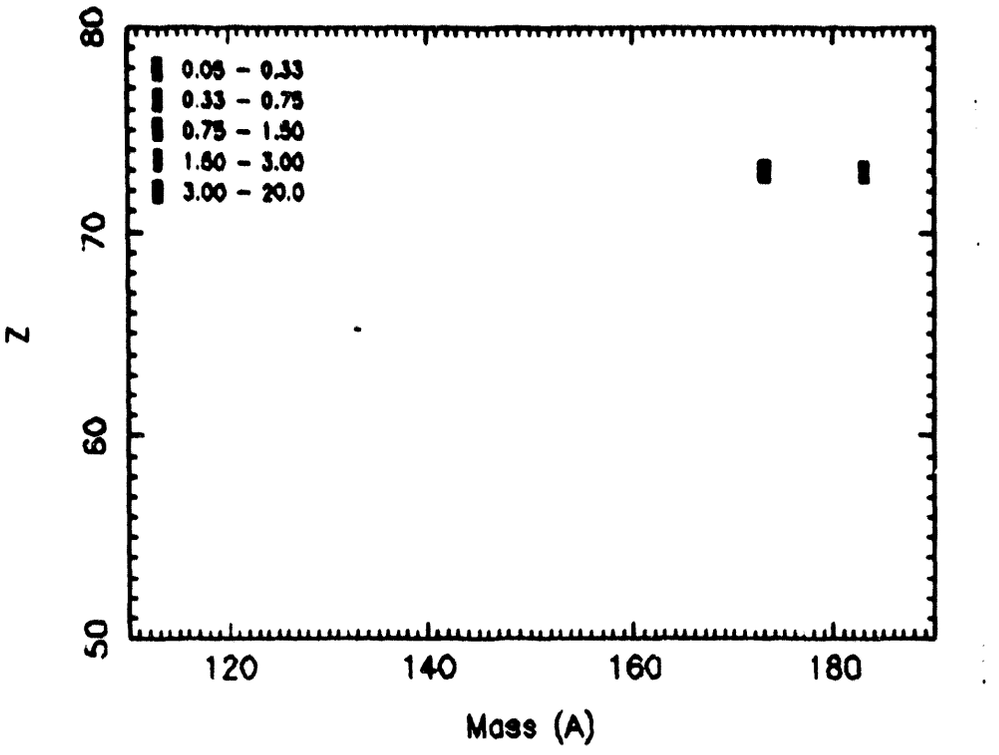

Fig. 19E. Ratio of measured yield to LAHET calculation for position 4B

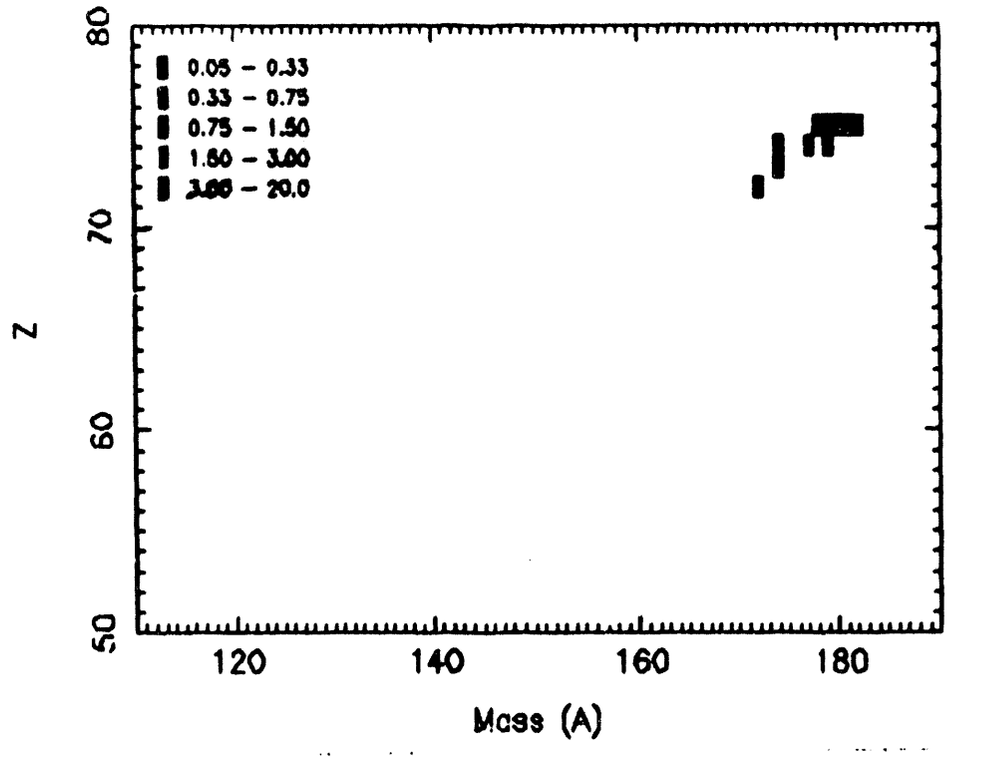

Fig. 19F. Ratio of measured yield to LAHET calculation for position 8B

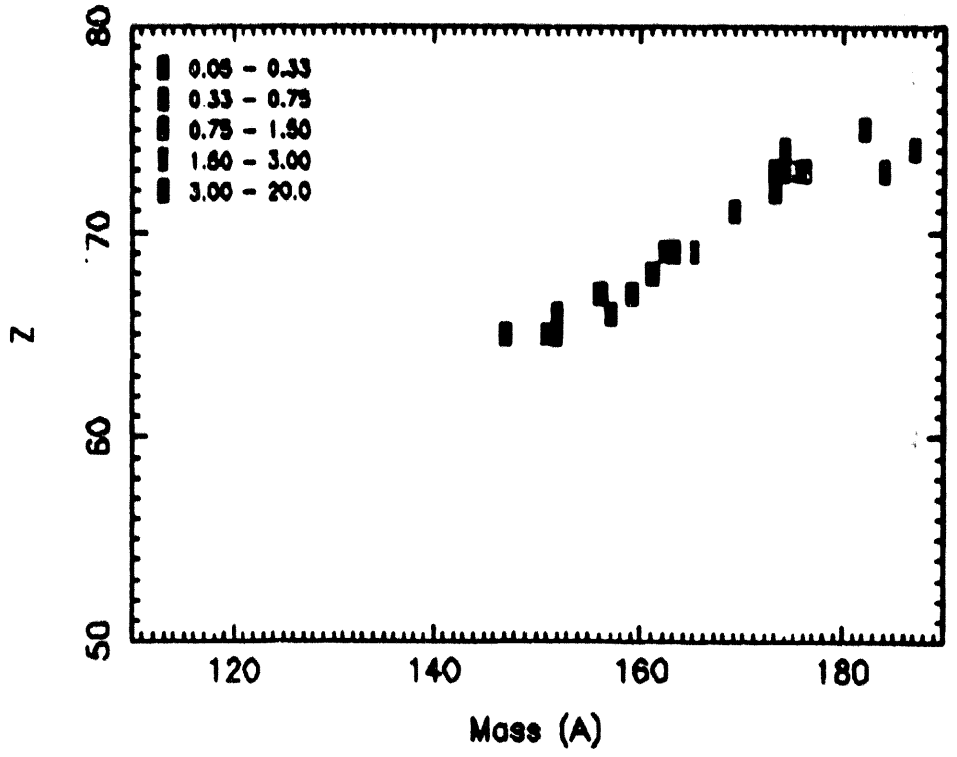

Fig. 20A Ratio of measured count rate to CINDER'90 prediction for position 2A

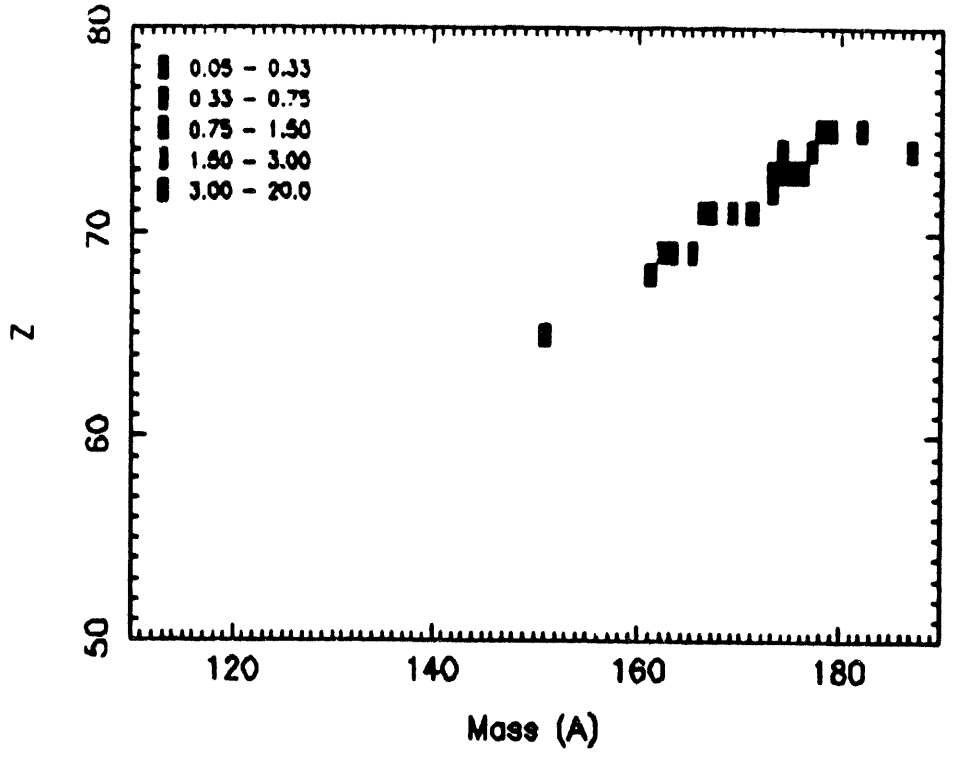

Fig. 20B. Ratio of measured count rate to CINDER'90 prediction for position 4A

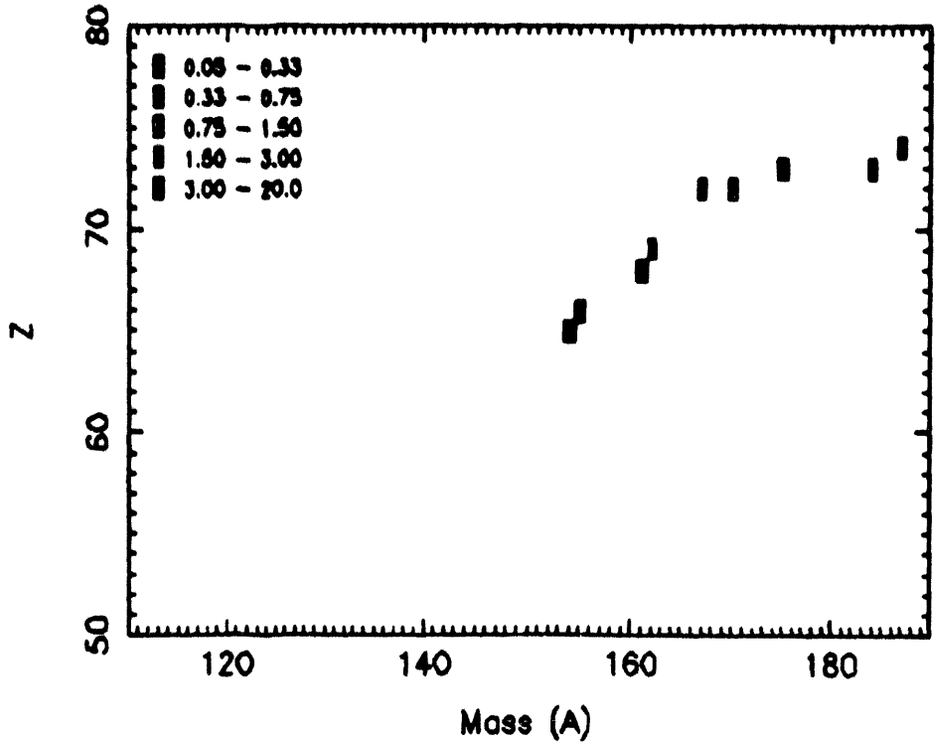

Fig. 20C. Ratio of measured count rate to CINDER'90 prediction for position 6A

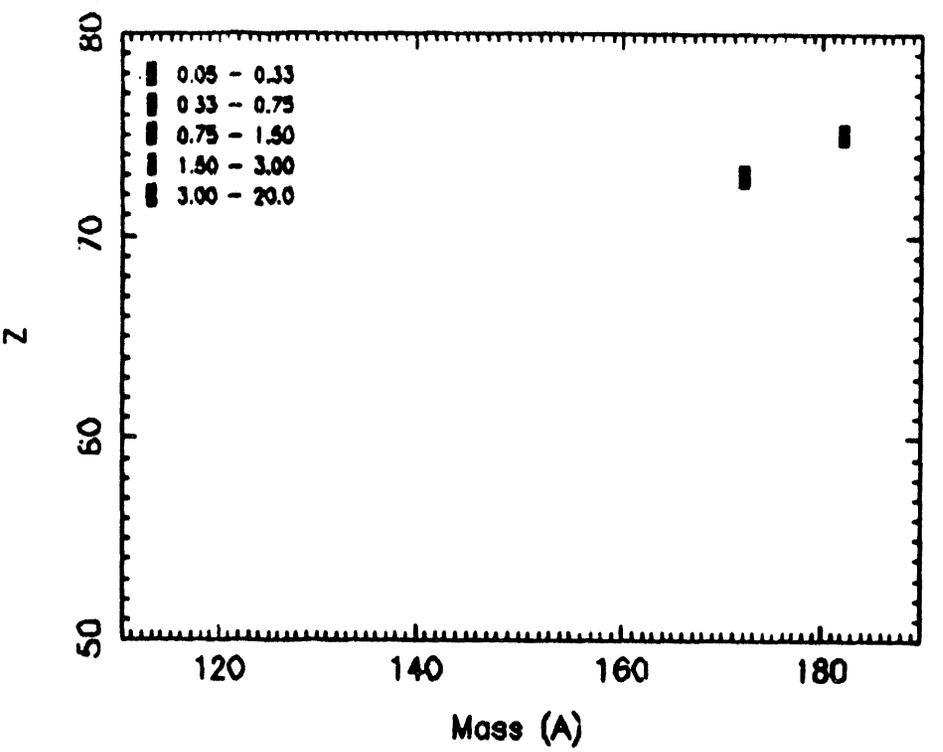

Fig. 20D. Ratio of measured count rate to CINDER'90 prediction for position 8A

As a summary of all the data, we compare the ratios of the measured yields to the LAHET or CINDER'90 calculations. Histograms of the ratios are shown in figure 21. This information in summarized in Table 5, which shows the percentage of calculated yields which are within a factor of two (from 0.5X to 1.5X) of the measured data.

Table 5 Percentage of calculated yields within a factor of two of measured value.

Position	LAHET	CINDER'90
2A	39%	62%
4A	37%	41%
6A	46%	43%
8A	67%	57%
4B	---	
8B	50%	
All	43%	51%

Fig 21 Histogram of distribution

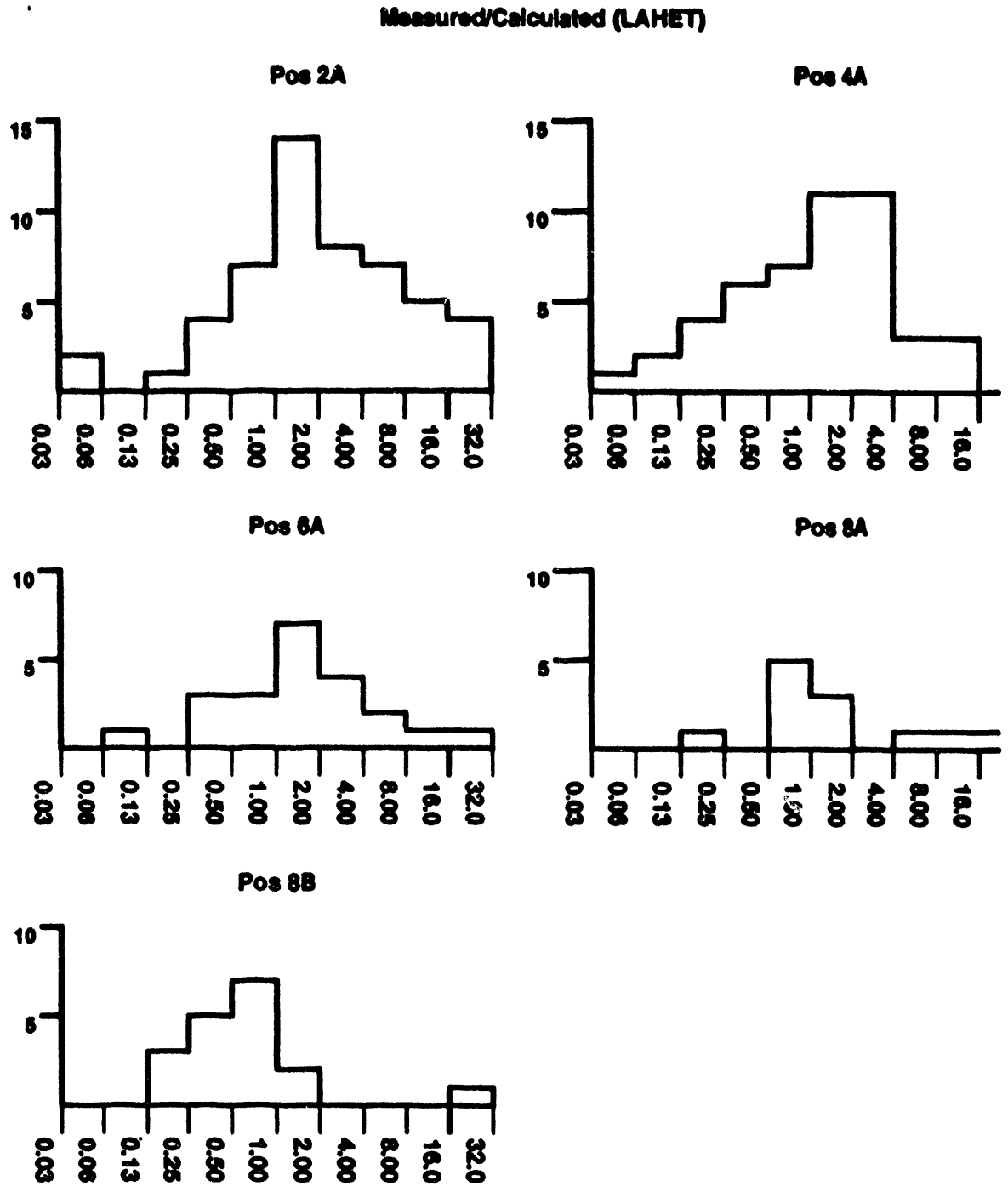

Figure 21A. Histogram of ratios of measured yields to LAHET calculations. Position 4B has too few points to plot.

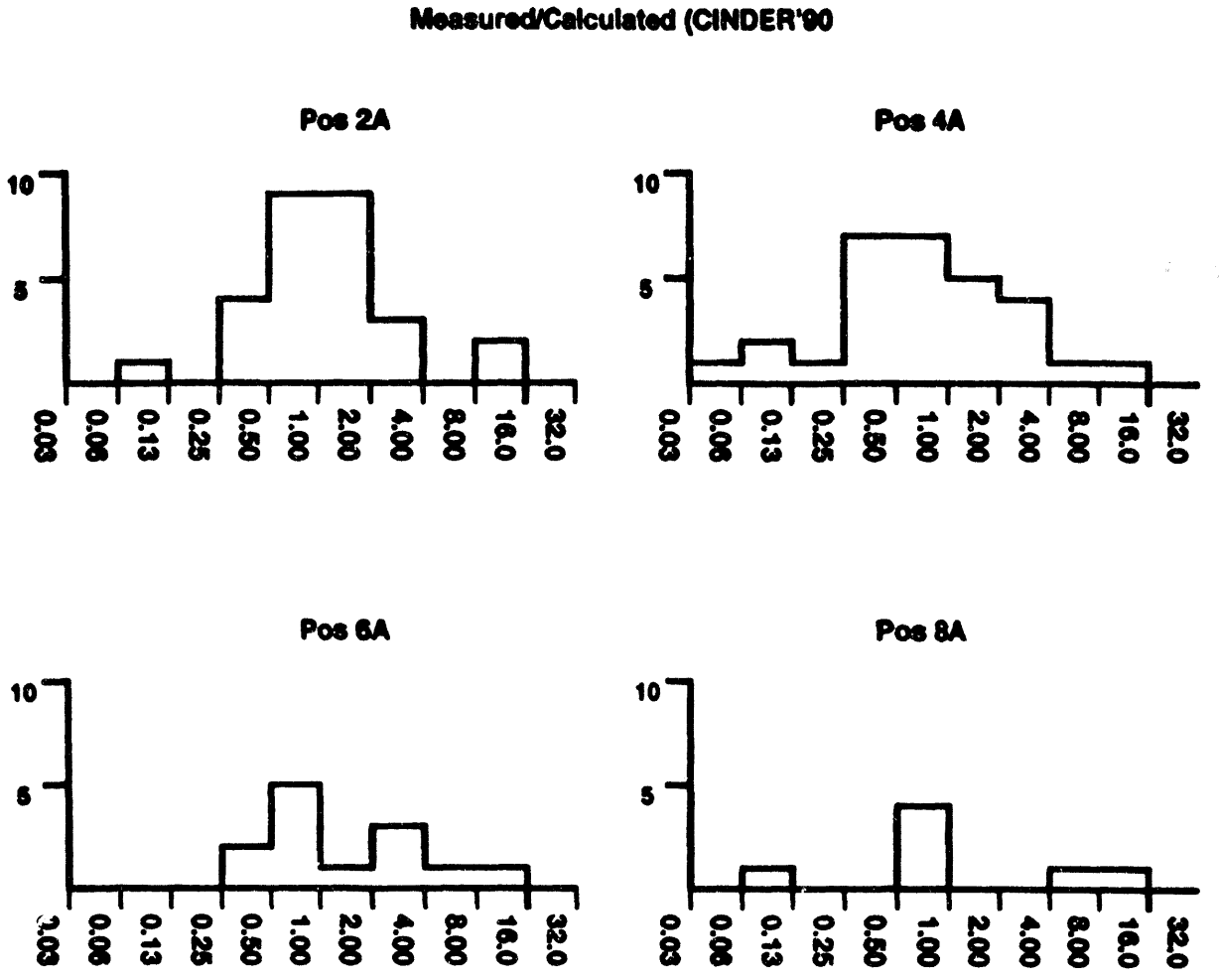

Figure 21B. Histogram of ratios of count rate to CINDER'90 calculations. Calculations were not available for positions 4B and 8B

5. Discussion

The information provided in this report summarizes our progress in benchmarking on ^{nat}W the radionuclide production code package that is used in APT target design and analysis. The experimental measurements were performed accurately and analysis of those data will provide valid information that will be invaluable in benchmarking spallation radionuclide production and the subsequent modification of those radionuclides through neutron interactions and decay. There was a vast quantity of data collected. Unfortunately, due to funding decreases in FY-1993, our ability to conduct analysis of the data was reduced severely. We concentrated on improving our computer analysis programs and their libraries, completing the necessary preanalysis checks on experimental procedure and data correction, such as detector energy calibration and efficiency determination, and then applying all of this to analysis of data from a single foil position.. During FY-1994, several additional computer programs were written to speed the analysis, to do parent corrections, and to compare the data directly to CINDER'90 calculations. The analysis focussed on all the on-axis foils and on off-axis foils in position 4B and 8B. The data presented here are the first to evaluate the production of short-half lived nuclei, and are also the first data of its kind for tungsten..

We analyzed the data in two ways. First, we extracted mass yields (in nuclei/cm3/proton) and compared them to LAHET calculations and the Summerer parameterization to try to undertand the underlying spallation physics. Next, we compared the results to calculations of CINDER'90, which use the raw spallation yields as input, but include low energy neutron capture and decay buildup. This represents our complete knowledge of the problem. An overall summary of the comparison is in Table 5, which shows 43% of the LAHET calculated yields are with a factor of two (from 0.5X to 1.5X) of the measurements, and 51% of the CINDER calculations are within the factor of two.

It is encouraging that the ratios are similar, and implies that the process of extracting spallation yields is probably very realistic. There are no obvious trends in (Z,A) in the disagreement, but rather the ratios seem randomly distributed, both in the comparison to LAHET and in the comparison to the CINDER'90 results. There is a possible very weak dependence on position, with the deeper foils being calculated slightly better than the foils closer to the front of the target. This could be conjectured to be due to better paramaterizations in the codes for lower incident energies, but the trend may not truly be significant. The final conclusion is that the calculations reproduce the data to within a factor of two, for 50% of the nuclei.

References

1. W. Amian, N.F. Peek, and D. Sterzenbach, "Production Rates of Spallation and Fission Products in Depleted Uranium and Natural Lead Targets Bombarded by 600 MeV and 1100 MeV Protons," Proceedings of the International Collaboration on Advanced Neutron Sources, ICANS-VII, September 13-16, 1983, Atomic Energy of Canada Limited, Report AECL-8488.
2. H. Takada, K. Hasegawa, T. Sasa, S. Meigo, and I. Kanno, "Integral Spallation Experiment with a Lead Assembly Irradiated with 500 MeV Protons," Proceedings of the 1992 Symposium on Nuclear Data, November 26-27, JAERI, Tokai, Japan, p72.
3. J.F. Breisneister, ed., "MCNP - A General Monte Carlo Code for Neutron and Photon Transport," LA-7396-M, Rev 2, Los Alamos National Laboratory, 1986.
4. T. Fukahori, S. Chiba, H. Takeda, N. Kishida, T. Watanabe, and N. Yamamuro, "Benchmark Calculations of Theoretical Calculation Codes for Nuclear Data Evaluations in the Intermediate Energy Region," Proceedings of the 1992 Symposium on Nuclear Data, November 26-27, JAERI, Tokai, Japan, p57.
5. N. P. Kocherov (Ed.), "Intermediate Energy Nuclear Data for Applications," Proceedings of the Advisory Group Meeting, International Atomic Energy Agency, 9-12 October, 1990, Vienna, Austria.
6. A. J. Koning, "Review of High Energy Data and Model Codes for Accelerator Based Transmutation for Accelerator Based Transmutation," NEA/NSC/Doc(92)12, June 1993.
7. A. J. Koning, "Requirements for an Evaluated Nuclear Data File for Accelerator Based Transmutation," NEA/NSC/Doc(93)6, June 1993.
8. R.E. Prael and H. Lichtenstein, "User Guide to LCS: The LAHET code System," Los Alamos National Laboratory, Sept. 15, 1989.
9. J.B. Cumming, et al., Nucl. Instr, and Meth. 180, 37 (1981).
10. Amersham QCD.1, Amersham Corp, Arlington Heights, IL.
11. R. Gunnink, computer code EFFIC (R. Gunnink, Fremont CA, 1991).
12. R. Gunnink and J.B. Niday, Computer code GAMANAL (Lawrence Livermore National Laboratory, Livermore CA, 1971. UCRL 51061. Modified for use at Los Alamos .
13. L. Spanier and P. Ekstrom, computer code GAMMAS (Dept. of Nuclear Physics, Lund University, Lund, Sweden, 1989).
14. W. Wilson, *et al.*,"Accelerator Transmutation Studies at Los Alamos with LAHET, MCNP, and CINDER'90," Los Alamos National Laboratory report LA-UR-93-3080.
15. W. Wilson, "Preliminary Results of Simulation Calculations of Tungsten Activation Experiments," Los Alamos National Laboratory Memorandum, T-2-M:93-3615.
16. K. Summerer, et al., Phys. Rev. C 42, 2546 (1990).

DATE
FILMED
9/13/94

END